NJC

Accepted Manuscript

This is an *Accepted Manuscript*, which has been through the Royal Society of Chemistry peer review process and has been accepted for publication.

Accepted Manuscripts are published online shortly after acceptance, before technical editing, formatting and proof reading. Using this free service, authors can make their results available to the community, in citable form, before we publish the edited article. We will replace this *Accepted Manuscript* with the edited and formatted *Advance Article* as soon as it is available.

You can find more information about *Accepted Manuscripts* in the Information for Authors.

Please note that technical editing may introduce minor changes to the text and/or graphics, which may alter content. The journal's standard Terms & Conditions and the Ethical guidelines still apply. In no event shall the Royal Society of Chemistry be held responsible for any errors or omissions in this *Accepted Manuscript* or any consequences arising from the use of any information it contains.

ROYAL SOCIETY OF CHEMISTRY

www.rsc.org/njc

NEW PYRIDAZINE-BASED BINUCLEAR NICKEL(II), COPPER(II) AND ZINC(II) COMPLEXES AS PROSPECTIVE ANTICANCER AGENTS

Ummer Muhammed Rafi[a], Dharmasivam Mahendiran[a], Azees Khan Haleel[a], Rakesh Pandeet Nankar[b], Mukesh Doble[b] and Aziz Kalilur Rahiman*[a].

[a]*Post-Graduate and Research Department of Chemistry, The New College (Autonomous), Chennai-600 014, India.*

[b] *Bioengineering and Drug Design Lab, Department of Biotechnology, Indian Institute of Technology Madras, Chennai-600 036, India.*

Abstract

A new class of pyridazine-based binuclear nickel(II), copper(II) and zinc(II) complexes of the type $[M_2(L^{1\text{-}3})_2](NO_3)_2$ (**1-9**) with tridentate Schiff base ligands 3-chloro-6-(salicylidenehydrazinyl)pyridazine (HL^1), 3-chloro-6-(5-nitrosalicylidenehydrazinyl)pyridazine (HL^2) and 3-chloro-6-(4-diethylaminosalicylidenehydrazinyl)pyridazine (HL^3) were synthesized and characterized. The molecular structure of the ligand HL^3 was determined by the single crystal XRD method. The geometry optimization and HOMO-LUMO energy level calculations were carried out using DFT studies. The electrochemical studies of nickel(II) (**1-3**) and copper(II) (**4-6**) complexes exhibit two irreversible one-electron reduction waves at $^1E_{pc}$ = −0.323 to −0.463 V and $^2E_{pc}$ = −0.634 to −0.790 V in cathodic potential region. The nickel(II) complexes (**1-3**) exhibit two irreversible one-electron oxidation waves at $^1E_{pa}$ = 1.009 to 1.025 V and $^2E_{pa}$ = 1.140 to 1.153 V in the anodic potential region. The spectroscopic data indicate that the ligands behave as a monoanionic tridentate ligand through the deprotonated phenolic oxygen and nitrogen atoms of azomethine group and pyridazine ring. The emission studies of the complexes at room temperature indicate the enhancement of fluorescence intensity than the ligands due to chelation-enhanced fluorescence effect (CHEF) suggesting the possible fluorescent probes of these Schiff bases for metal ions. *In vitro* cytotoxic activity of all the complexes were assessed against one breast cancer (MDA-MB-231) and one healthy

myoblast non-cancer (L-6) cell lines. The IC_{50} values of complexes **3** and **9** indicate their high cytotoxicity against MDA-MB-231 cells when compared to the standard drug cisplatin suggesting that these complexes may act as potential antitumor agents. Nuclear chromatin cleavage have also been observed with AO/EB staining assay. Flow cytometry analysis of complexes **3** and **9** revealed cell cycle arrest in the S phase. Molecular docking studies were also carried out for the complexes **3** and **9** to find their binding affinity with protein EGFR kinase.

Keywords: Schiff base, X-ray crystal structure, Emission properties, Electrochemical studies, Anticancer activity, Apoptosis, Cell cycle arrest.

*Corresponding author. Tel.: +91 44 2835 0297; Fax: + 91 44 2835 2883.

E-mail: akrahmanjkr@gmail.com

1. Introduction

Transition metal complexes with bi, tri and tetradentate Schiff base ligands containing oxygen and nitrogen donor atoms have the ability to possess unusual configuration and remarkable biomedical activities that could be used to develop new metal-based anticancer agents [1]. Pyridazine, a type of heterocyclic diazine has wide applications in drug design [2], agrochemical activities [3] and has also been used as ligands in co-ordination chemistry. There have been numerous systems such as acyclic ligands [4], coordination polymers [5], cryptands [6] and also macrocycles [7] in which pyridazine units have been incorporated. Over the past years, pyridazine derivatives have been extensively studied and have shown a wide range of pharmacological activities such as antidepressant [8], antibacterial [9], COX-2 inhibitor [10] and anticancer activities [11]. The introduction of new substituent or functional groups at various positions on aromatic or heteroaromatic fragments of a potential drug might lead to changes in its molecular shape that allows optimum binding to the receptor, as well as its physico-chemical properties that affect drug distribution and metabolism [12].

Pyridazine-based transition metal complexes have received immense attention in co-ordination chemistry due to their great structural diversity [13, 14]. A unique chemical behavior can be expected due to the different electronic ligand properties when compared to pyridine systems. When compared to pyridine, the presence of two N-donor atoms in pyridazine leads to a decrease in electron donor abilities, which is reflected in significant lower pKa values (2.24 for parent pyridazine whereas 5.25 for pyridine) [15]. In many cases, pyridazine-based ligands are capable of coordinating two metal atoms when they are in close proximity through their diazine fragments and are substituted in 3- and 6- position with two donors to exploit the chelate effect and thus increase the binding tendency of the electron-poor second nitrogen donor. However, these systems have been observed only in pyridazine ligands with preferred compartmental or in macrocyclic systems [16, 17]. Thus, Pyridazine without adjacent coordination sites act mostly as monodentate ligands comparable to pyridine [18]. Pyridazine with only one additional donor next to a ring nitrogen atom leading to bi- or tridentate ligands have been less investigated in coordination chemistry [19].

Cancer is the second leading cause of human deaths after cardiovascular diseases [20]. Though chemotherapy is the mainstay of cancer treatment, the use of available chemotherapeutics still suffers from major limitations such as lack of selectivity of cancer tissues, bringing unwanted side effects and the acquisition by cancer cells of multiple-drug resistance [21]. Therefore, the search for new drugs, which can selectively target the tumor cells is today's goal of cancer therapy. Introduction of appropriate heterocycles into a lead compound is a common strategy in the drug discovery process. Hence, our strategy was to synthesize three new pyridazine-based Schiff base ligands that contain additional donor sites at the 3-position of the heterocycles, whereas the 6-position was substituted by a non-coordinating group. The three Schiff base ligands were prepared by the condensation of 3-chloro-6-hydrazinopyridazine with salicylaldehyde, 5-nitrosalicylaldehyde or

4-(diethylamino)salicylaldehyde. Using these ligands, a new series of nickel(II), copper(II) and zinc(II) complexes were synthesized. *In vitro* anticancer activities of the complexes have been screened against one human breast cancer (MDA-MB-231) and one healthy non-cancer myoblast (L-6) cell lines by MTT assay. The cell death or apoptotic studies was carried out by using AO/EB staining method and the cell cycle arrest was performed by flow cytometry analysis.

2. Experimental

2.1. General methods and materials

The compound 3-chloro-6-hydrazinopyridazine was prepared by following the procedure described in the literature [22]. 3,6-dichloropyridazine, salicylaldehyde, 5-nitrosalicylaldehyde, 4-(diethylamino)salicylaldehyde and metal(II) nitrates were purchased from Aldrich and used without further purification. Solvents used in the synthesis were dried and purified before being used according to standard procedure [23]. The melting points were determined using electro thermal capillary apparatus and reported as uncorrected values. Elemental analyses (CHN) were performed on a Carlo Erba model 1106 elemental analyzer. IR spectra were recorded on a Perkin-Elmer 297 spectrophotometer using KBr pellets in the range of 4000−400 cm^{-1}. NMR spectra were recorded on a Bruker Avance spectrometer using DMSO-d_6 as solvent (400 MHz for ^{1}H and 100 MHz for ^{13}C NMR). ESI mass spectra were recorded on a Thermo Scientific Orbitrap Elite Mass spectrometer. UV-Vis spectra were recorded on a Cary 100 version 11.1 spectrophotometer using DMSO as solvent. The luminescence spectra were recorded on FluoroMax 4C-TCSPC fluorescence spectrofluorometer at room temperature using DMSO as solvent. X-Band EPR spectra were recorded at 25 °C on a Varian EPR-E 112 spectrometer using 2,2′-diphenyl-1-picrylhydrazyl (DPPH) as the reference. The room temperature magnetic moment was measured on a PAR (model-155) vibrating sample magnetometer. Molar conductivity was measured with an Elico

digital conductivity bridge model CM-88, using a freshly prepared DMF solution of the complexes. Cyclic voltammograms were obtained on CHI 602D (CH Instruments Co., USA) electrochemical analyzer under oxygen free conditions using a three-electrode cell with a DMF solution of TBAP (0.1 M) as the supporting electrolyte. A Pt wire, glassy carbon and the Ag/AgCl electrodes (saturated KCl solution) were used as counter, working and reference electrodes, respectively. A ferrocene/ferrocenium (Fc/Fc^+) couple was used as an internal standard. The reported potentials were relative to the Ag/AgCl electrode and $E_{1/2}$ of the Fc/Fc^+ couple. The concentration of complex solutions was taken around 1.0×10^{-3} M and the scan rate was 100 mVs^{-1}.

2.2. Synthesis of pyridazine-based ligands (HL^{1-3})

All the ligands were synthesized by the [1+1] Schiff base condensation reaction.

3-chloro-6-(salicylidenehydrazinyl)pyridazine (HL^1)

An ethanolic solution (30 mL) of salicylaldehyde (0.61 mL, 5 mmol) was slowly added to an ethanolic solution (30 mL) of 3-chloro-6-hydrazinopyridazine (0.72 g, 5 mmol) with constant stirring in the presence of acetic acid (3 drops) as a catalyst under the nitrogen atmosphere. The stirring was continued for 1 h and refluxed for 2 h. The product was collected by filtration, washed with ethanol and dried in vacuo.

Yield: 1.02 g (82.04%), mp: 252 °C. Colour: yellow. Anal. calcd. for $C_{11}H_9N_4OCl$, (FW: 248.67): C, 53.13; H, 3.65: N, 22.53. Found: C, 53.08; H, 3.62; N, 22.52%. Selected IR data (KBr, cm^{-1}): 3452 ν(−OH), 3218 ν(−NH), 1628 ν(−C=N), 1283 ν(Ar−O), 1533 ν(−N=N). UV-Vis (DMSO) λ_{max} (nm) (ε ($M^{-1}cm^{-1}$)): 339 (19,616). ^{1}H NMR (400 MHz, DMSO-d_6) : δ 11.63 (s, 1H, phenolic proton), 10.17 (s, 1H, NH), 8.43 (s, 1H, azomethine –CH=N), 7.72 (d, 1H, Ar−H, J = 7.6 Hz), 7.66 (d, 1H, Ar_{pdz}−H, J = 9.6 Hz), 7.55 (d, 1H, Ar_{pdz}−H, J = 9.6 Hz), 7.22 (t, 1H, Ar−H, J = 7.6 Hz), 6.89 (m, 2H, Ar−H). ^{13}C NMR (400 MHz, DMSO-d_6): δ 158.86, 156.44, 147.75, 140.76, 130.88, 130.41, 126. 99, 119.84, 116.57,

116.31. ^{13}C (DEPT-135) NMR (400 MHz, DMSO-d_6): δ 140.75, 130.89, 130.41, 126.98, 119.85, 116.57, 116.31 (methine carbons).

3-chloro-6-(5-nitrosalicylidenehydrazinyl)pyridazine (HL^2)

The solid ligand HL^2 was prepared by following the procedure similar to that of HL^1 using 5-nitrosalicylaldehyde (0.84 g, 5 mmol) instead of salicylaldehyde.

Yield: 1.27 g (86.49%), mp: 260 °C. Colour: yellow. Anal. calcd. for $C_{11}H_8N_5O_3Cl$, (FW: 293.67): C, 44.99; H, 2.75: N, 23.85. Found: C, 44.95; H, 2.72; N, 23.84%. Selected IR data (KBr, cm^{-1}): 3452 ν(−OH), 3208 ν(−NH), 1629 ν(−C=N), 1290 ν(Ar−O), 1518 ν(−N=N). UV-Vis (DMSO) λ_{max} (nm) (ε ($M^{-1}cm^{-1}$)): 336 (20,838), 465 (2,110). ^{1}H NMR (400 MHz, DMSO-d_6) : δ 11.80 (s, 1H, phenolic proton), 11.60 (s, 1H, NH), 8.51 (s, 1H, Ar−H), 8.33 (s, 1H, azomethine –CH=N), 8.04 (d, 1H, Ar−H, J = 9.2 Hz), 7.62 (d, 1H, Ar−H, J = 9.2 Hz), 7.57 (d, 1H, Ar_{pdz}−H, J = 9.6 Hz), 7.00 (d, 2H, Ar_{pdz}−H, J = 9.2 Hz). ^{13}C NMR (400 MHz, DMSO-d_6): δ 161.79, 158.92, 148.21, 140.56, 137.08, 130.66, 126.16, 122.15, 121.65, 117.07, 116.56. ^{13}C (DEPT-135) NMR (400 MHz, DMSO-d_6): δ 137.07, 130.66, 126.16, 121.06, 117.07, 116.58 (methine carbons).

3-chloro-6-(4-(diethylamino)salicylidenehydrazinyl)pyridazine (HL^3)

The solid ligand HL^3 was prepared by following the procedure similar to that of HL^1 using 4-(diethylamino)salicylaldehyde (0.97 g, 5 mmol) instead of salicylaldehyde.

Yield: 1.26 g (78.80%), mp: 250 °C. Colour: Yellow. Anal. calcd. for $C_{15}H_{18}N_5OCl$, (FW: 319.79): C, 56.34; H, 5.67: N, 21.90. Found: C, 56.29; H, 5.63; N, 21.89%. Selected IR data (KBr, cm^{-1}): 3468 ν(−OH), 3194 ν(−NH), 1631 ν(−C=N), 1282 ν(Ar−O), 1535 ν(−N=N). UV-Vis (DMSO) λ_{max} (nm) (ε ($M^{-1}cm^{-1}$)): 371 (38,063). ^{1}H NMR (400 MHz, DMSO-d_6) : δ 11.27 (s, 1H, phenolic proton), 10.18 (s, 1H, NH), 8.23 (s, 1H, azomethine –CH=N), 7.60 (d, 1H, Ar_{pdz}−H, J = 9.2 Hz), 7.35 (d, 2H, Ar−H, J = 8.8 Hz), 6.25 (d, 1H, Ar_{pdz}−H, J = 8.8 Hz), 6.12 (s, 1H, Ar−H), 3.36 (q, 4H, CH_2, J = 6.8 Hz), 1.18 (t, 6H, CH_3,

J = 6.8 Hz). ^{13}C NMR (400 MHz, DMSO-d_6): δ 158.53, 158.42, 150.07, 146.98, 143.89, 130.21, 129.56, 115.88, 108.11, 104.33, 97.95, 44.26, 13.03. ^{13}C (DEPT-135) NMR (400 MHz, DMSO-d_6): δ143.88, 130.21, 129.55, 115.88, 104.33, 97.94 (methine carbons), 44.26 (methylene carbons), 13.03 (methyl carbons).

2.3. General procedure for the synthesis of pyridazine-based binuclear metal(II) complexes

The binuclear nickel(II), copper(II) and zinc(II) complexes were prepared by following the same procedure as given below: An ethanolic solution (30 mL) of $Ni(NO_3)_2.6H_2O$ (0.29 g, 1.2 mmol), $Cu(NO_3)_2.3H_2O$ (0.29 g, 1.2 mmol) or $Zn(NO_3)_2.6H_2O$ (0.36 g, 1.2 mmol) was added to an equimolar amount of appropriate ligand ($HL^{1\text{-}3}$, 1.2 mmol) in ethanol (30 mL) with constant stirring while a colour change was immediately observed. The stirring was continued for 30 min and refluxed on a water bath for additional 3 h, filtered while hot, and the filtrate was allowed to stand at room temperature for few days. The solid complexes obtained were recrystallized using hot ethanol.

$[Ni_2(L^1)_2](NO_3)_2$ (1)

Yield: 0.51 g (58%). Colour: Brown. Anal. calcd. for $C_{22}H_{16}N_{10}O_8Cl_2Ni_2$, (FW: 736.72): C, 35.87; H, 2.19: N, 19.01. Found: C, 35.83; H, 2.17; N, 19.00%. Selected IR data (KBr, cm^{-1}): 3220 ν(−NH), 1610 ν(−C=N), 1264 ν(Ar−O), 1555 ν(−N=N), 1383 ν(NO_3^-). UV-Vis (DMSO) λ_{max} (nm) (ε ($M^{-1}cm^{-1}$)): 263 (15,007), 298 (14,001), 418 (5,336), 588 (970). ESI-MS (*m/z*): 609.959 ($[NiL^1]_2^+$; 60%), 304.972 ($[NiL^1]^+$; 100%). Conductance (Λ_M, $\Omega^{-1}cm^2mol^{-1}$) in DMF: 161.

$[Ni_2(L^2)_2](NO_3)_2$ (2)

Yield: 0.58 g (58%). Colour: Brown. Anal. calcd. for $C_{22}H_{14}N_{12}O_{12}Cl_2Ni_2$, (FW: 826.71): C, 31.96; H, 1.71: N, 20.33. Found: C, 31.93; H, 1.69; N, 20.32%. Selected IR data (KBr, cm^{-1}): 3219 ν(−NH), 1601 ν(−C=N), 1257 ν(Ar−O), 1552 ν(−N=N), 1384 ν(NO_3^-). UV-Vis (DMSO) λ_{max} (nm) (ε ($M^{-1}cm^{-1}$)): 233 (11,220), 301 (15,239), 412

(14,509), 594 (677). ESI-MS (*m/z*): 699.925 ($[NiL^2]_2^+$; 53%), 349.962 ($[NiL^2]^+$; 100%). Conductance (Λ_M, $\Omega^{-1}cm^2mol^{-1}$) in DMF: 131.

$[Ni_2(L^3)_2](NO_3)_2$ (3)

Yield: 0.55 g (52%). Colour: Brown. Anal. calcd. for $C_{30}H_{34}N_{12}O_8Cl_2Ni_2$, (FW: 878.96): C, 40.99; H, 3.89: N, 19.12. Found: C, 40.96; H, 43.87%; N, 19.11. Selected IR data (KBr, cm^{-1}): 3220 ν(−NH), 1604 ν(−C=N), 1243 ν(Ar−O), 1565 ν(−N=N), 1384 ν(NO_3^-). UV-Vis (DMSO) λ_{max} (nm) (ε ($M^{-1}cm^{-1}$)): 311 (10,928), 423 (9,115), 572 (778). ESI-MS (*m/z*): 754.095 ($[NiL^3]_2^+$; 67%), 376.052 ($[NiL^3]^+$; 100%). Conductance (Λ_M, $\Omega^{-1}cm^2mol^{-1}$) in DMF: 148.

$[Cu_2(L^1)_2](NO_3)_2$ (4)

Yield: 0.58 g (65%). Colour: Green. Anal. calcd. for $C_{22}H_{16}N_{10}O_8Cl_2Cu_2$, (FW: 746.42): C, 35.40; H, 2.16: N, 18.77. Found: C, 35.37; H, 2.14; N, 18.76%. Selected IR data (KBr, cm^{-1}): 3224 ν(−NH), 1605 ν(−C=N), 1250 ν(Ar−O), 1545 ν(−N=N), 1384 ν(NO_3^-). UV-Vis (DMSO) λ_{max} (nm) (ε ($M^{-1}cm^{-1}$)): 275 (15,044), 398 (8,370), 437 (2,504), 655 (734). ESI-MS (*m/z*): 620.930 ($[CuL^1]_2^+$; 64%), 309.967 ($[CuL^1]^+$; 100%). Conductance (Λ_M, $\Omega^{-1}cm^2mol^{-1}$) in DMF: 152. $g_{\|} = 2.254$, $g_{\perp} = 2.092$. $\mu_{eff} = 1.59$ B.M.

$[Cu_2(L^2)_2](NO_3)_2$ (5)

Yield: 0.60 g (60%). Colour: Green. Anal. calcd. for $C_{22}H_{14}N_{12}O_{12}Cl_2Cu_2$, (FW: 836.42): C, 31.60; H, 1.69: N, 20.10. Found: C, 31.56; H, 1.67; N, 20.08%. Selected IR data (KBr, cm^{-1}): 3115 ν(−NH), 1612 ν(−C=N), 1240 ν(Ar−O), 1546 ν(−N=N), 1387 ν(NO_3^-). UV-Vis (DMSO) λ_{max} (nm) (ε ($M^{-1}cm^{-1}$)): 263 (20,602), 372 (23,928), 441 (16,571), 650 (436). ESI-MS (*m/z*): 710.902 ($[CuL^2]_2^+$; 40%), 354.955 ($[CuL^2]^+$; 100%). Conductance (Λ_M, $\Omega^{-1}cm^2mol^{-1}$) in DMF: 172. $g_{\|} = 2.262$, $g_{\perp} = 2.088$. $\mu_{eff} = 1.63$ B.M.

$[Cu_2(L^3)_2](NO_3)_2$ (6)

Yield: 0.49 g (46%). Colour: Green. Anal. calcd. for $C_{30}H_{34}N_{12}O_8Cl_2Cu_2$, (FW: 888.66): C, 40.55; H, 3.86: N, 18.91. Found: C, 40.51; H, 3.82; N, 18.90%. Selected IR data (KBr, cm^{-1}): 3212 ν(−NH), 1608 ν(−C=N), 1249 ν(Ar−O), 1568 ν(−N=N), 1384 ν(NO_3^-). UV-Vis (DMSO) λ_{max} (nm) (ε ($M^{-1}cm^{-1}$)): 308 (13,725), 411 (10,200), 611 (820). ESI-MS (*m/z*): 764.095 ($[CuL^3]_2^+$; 61%), 381.041 ($[CuL^3]^+$; 100%). Conductance (Λ_M, $\Omega^{-1}cm^2mol^{-1}$) in DMF: 166. $g_{\|} = 2.249$, $g_{\perp} = 2.058$. $\mu_{eff} = 1.62$ B.M.

$[Zn_2(L^1)_2](NO_3)_2$ (7).

Yield: 0.51 g (57%). Colour: Yellow. Anal. calcd. for $C_{22}H_{16}N_{10}O_8Cl_2Zn_2$, (FW: 750.11): C, 35.23; H, 2.15: N, 18.67. Found: C, 35.19; H, 2.13; N, 18.66%. Selected IR data (KBr, cm^{-1}): 3217 ν(−NH), 1615 ν(−C=N), 1277 ν(Ar−O), 1551 ν(−N=N), 1380 ν(NO_3^-, uncoordinated). UV-Vis (DMSO) λ_{max} (nm) (ε ($M^{-1}cm^{-1}$)): 338 (22,461). ESI-MS (*m/z*): 625.932 ($[ZnL^1]_2^+$; 58%), 310.968 ($[ZnL^1]^+$; 100%). Conductance (Λ_M, $\Omega^{-1}cm^2mol^{-1}$) in DMF: 153.

$[Zn_2(L^2)_2](NO_3)_2$ (8)

Yield: 0.61 g (60%). Colour: Yellow. Anal. calcd. for $C_{22}H_{14}N_{12}O_{12}Cl_2Zn_2$, (FW: 840.11): C, 31.45; H, 1.68: N, 20.01. Found: C, 31.42; H, 1.67; N, 19.99%. Selected IR data (KBr, cm^{-1}): 3208 ν(−NH), 1613 ν(−C=N), 1251 ν(Ar−O), 1554 ν(−N=N), 1384 ν(NO_3^-, uncoordinated). UV-Vis (DMSO) λ_{max} (nm) (ε ($M^{-1}cm^{-1}$)): 326 (16,285). ESI-MS (*m/z*): 715.962 ($[ZnL^2]_2^+$; 49%), 355.954 ($[ZnL^2]^+$; 100%). Conductance (Λ_M, $\Omega^{-1}cm^2mol^{-1}$) in DMF: 159.

$[Zn_2(L^3)_2](NO_3)_2$ (9)

Yield: 0.57 mg (53%). Colour: Yellow. Anal. calcd. for $C_{30}H_{34}N_{12}O_8Cl_2Zn_2$, (FW: 892.35): C, 40.38; H, 3.84: N, 18.84. Found: C, 40.34; H, 3.81; N, 18.83%. Selected IR data (KBr, cm^{-1}): 3220 ν(−NH), 1603 ν(−C=N), 1243 ν(Ar−O), 1562 ν(−N=N), 1382

ν(NO_3^-, uncoordinated). UV-Vis (DMSO) λ_{max} (nm) (ε ($M^{-1}cm^{-1}$)): 319 (19,240). ESI-MS (*m/z*): 768.081 ($[ZnL^3]_2^+$; 65%), 382.043 ($[ZnL^3]^+$; 100%). Conductance (Λ_M, $\Omega^{-1}cm^2mol^{-1}$) in DMF: 147.

2.4. X-Ray crystallographic analysis

Single crystals suitable for X-ray analysis were obtained by the slow evaporation of HL^3 in DMSO at room temperature. The yellow coloured crystal was cut to suitable size (0.35 × 0.30 × 0.20 mm) and mounted on Kappa Apex2 CCD diffractometer equipped with graphite monochromated Mo Kα radiation in the wavelength (λ) of 0.71073 Å at room temperature. The intensity data were collected using ω and φ scans with frame width of 0.5°. The frame integration and data reduction were performed using Bruker SAINT-Plus (Version 7.06a) software. The multi-scan absorption corrections were applied to the data using SADABS program [24]. The structure was solved by using SIR92 [25] and the full matrix least squares refinement on F^2 was performed using SHELXL-97 program [26]. The molecular graphics, hydrogen bonding and packing figures were generated by using the software ORTEP 3.0 [27]. The final R-value was 0.0873, and the final electrodensity map contains maximum and minimum peak heights of 0.341 and −0.409 $eÅ^{-3}$, respectively.

2.5. Computational details

Gaussian 03 [28] software package was used for theoretical calculations. The quantum chemical calculations were performed applying DFT method, with Becke-3-Lee-Yang-Parr (B3LYP) supplemented with the standard 6-31G(d) basis set [29]. The optimized geometry corresponding to the minimum on the potential energy surface has been obtained by solving self-consistent field equation iteratively.

2.6. Anticancer activity

2.6.1. Cell viability assay

The rat myoblast non-cancer (L-6) and human breast cancer (MDA-MB-231) cell lines were purchased from National Center for Cell Science (NCCS) Pune, India. Both the cell lines were grown in Dulbecco's Modified Eagle's Medium (DMEM) (Himedia, India) containing 10% fetal bovine serum (FBS) (Gibco, Life Technologies Corporation, Grand Island, NY, USA) and 1% antibiotic-antimycotic solution 100X (Himedia) in a humidified atmosphere with 5% of CO_2 at 37 °C. Stock solutions of all the compounds were prepared in cell culture grade DMSO (Himedia).

Effect of treatment of compounds on cell viability was determined using tetrazolium dye, 3-(4,5-dimethylthiazol-2-yl)-2,5-diphenyltetrazolium bromide (MTT) assay as reported earlier [30]. Cells were seeded in a 96 well plate at a density of 5000 cells/well. When cells reached 60% confluency, they were treated with increasing concentrations of complexes (3.9, 7.8, 15.6, 31.25, 62.5, 125, 250 and 500 μM) for 24 h. After 24 h, the medium was replaced with 0.5 mg/mL of MTT and incubated for 4 h. Live cells have the ability to reduce yellow soluble MTT dye to blue insoluble formazan crystals. The medium was removed and formazan crystals were dissolved by adding DMSO (200 μL/well). The optical density of each well at 570 nm was measured in a multimode plate reader (Enspire, Perkin Elmer, Waltham, MA, USA). The % cell viability for each treatment was calculated using the following equation,

$$\text{Cell viability (\%)} = \frac{A_{570\ \text{nm}}\ \text{of treated cells}}{A_{570\ \text{nm}}\ \text{of control cells}} \times 100$$

IC_{50}, the concentration of compounds required to attain 50% of cell viability (relative to control), for each compound was estimated by non-linear fitting of curve obtained by plotting % cell viability *verses* log concentration (GraphPad Prism, Version 5.04).

2.6.2. Cell clonogenic assay

Cell clonogenic assay was preformed as described earlier [31]. MDA-MB-231 cells were seeded in a 6 well plate at a density of 400 cells/well/2 mL. Cells were grown for 7 days until the colonies were formed. After 7 days, cells were treated with 75 μM of complex **3** or 37 μM of complex **9** (IC_{50} concentrations of complexes). Treatment was stopped after 24 h and cells were allowed to grow for another 7 days. The media was aspirated and cells were washed with PBS (pH 7.4) to remove the detached cells. Colonies of cells were fixed in ice cold methanol for 15 min and stained with 0.5% crystal violet solution.

2.6.3. Apoptosis studies

Cell apoptosis was assessed using the AO/EB fluorescent staining method. MDA-MB-231 cells were seeded in a 12 well plate at a density of 4×10^4 cells/well/mL. Cells were allowed to grow for 24 h. Cells were treated with 75 μM of complex **3** or 37 μM of complex **9** (IC_{50} concentration of complexes) for 24 h. After 24 h, cells were harvested with trypsin-EDTA solution and resuspended in 100 μL of PBS (pH 7.4). The morphological changes in the cells after treatment with complexes **3** and **9** were assessed by fluorescence microscopy after staining with AO/EB. 10 μL of cell suspension was mixed with 10 μL of freshly prepared AO/EB staining solution (50 μg/mL) and obseved under Olympus 1X-51 inverted fluoroscent microscope at 10X magnification and images were taken using OptikaView Version 2.8.3.0 software. The cells were counted within 20 min and the percentage of necrotic and apoptotic cells were calculated using the following formula [32],

$$\text{Apoptotic cells (\%)} = (VA + NVA)/(VN + VA + NVN + NVA) \times 100$$

$$\text{Necrotic cells (\%)} = (NVN)/(VN + VA + NVN + NVA) \times 100$$

where

VN = Viable cells with normal nuclei (bright green chromatin having organized structure),

VA = Viable cells with apoptotic nuclei (highly condensed or fragmented bright green chromatin)

NVN = Nonviable cells with normal nuclei (bright orange chromatin having organized structure) and

NVA = Nonviable cells with apoptotic nuclei (highly condensed or fragmented bright orange chromatin).

2.6.4. Flow cytometry for cell cycle analysis

MDA-MB-231 cells were seeded in a 6 well plate at a density of 2×10^5 cells/well/2 mL. When reached 60% confluency, cells were treated with 75 μM of complex **3** or 37 μM of complex **9** (IC_{50} concentration of complexes) for 24 h. Then, the cells were trypsinised, washed with phosphate buffer saline (pH 7.4) and incubated with RNAase A (10 μg/mL) at room temperature for 30 min followed by staining with propidium iodide (5 μg/mL) for 10 min. The percentage of cells in different phases of cell cycle was determined using BD FACSVerse flow cytometer and BD FACSuite software (BD Biosciences) [32].

2.7. Molecular docking studies with protein EGFR kinase

Molecular docking studies were carried out using the AutoDock Tools (ADT) version 1.5.6 and AutoDock version 4.2.5.1 docking programmes. The structures of the complexes **3** and **9** were converted into PDB format from mol format by OPENBABEL. The crystal structure of the epidermal growth factor receptor (EGFR) protein tyrosine kinase (PDB ID: 1M17) was downloaded from the protein data bank (http://www.rcsb.org./pdb). The receptor (EGFR) and the ligand (complexes) files were prepared using AutoDock Tools. First, all the heteroatoms including water molecules were deleted while polar hydrogen atoms and Kollman charges were added to the receptor molecule, then rotatable bonds in ligands were assigned. All other bonds were allowed to rotate. The EGFR was enclosed in a box with number of grid points in x × y × z directions, 60 × 60 × 60 and a grid spacing of 0.4 Å.

Lamarckian genetic algorithms, as implemented in AutoDock, was employed to perform docking calculations. All other parameters were default settings. For each of the docking cases, the lowest energy docked conformation, according to the Autodock scoring function, was selected as the binding mode. Visualization of the docked position has been done by using PyMOL molecular graphics program.

3. Results and discussion

3.1. Synthesis of ligands and complexes

The pyridazine-based ligands (HL^{1-3}) were synthesized in a two step procedure, in which 3-chloro-6-hydrazinopyridazine was prepared by refluxing 3,6-dichloropyridazine with hydrazine hydrate in boiling aqueous ammonia followed by condensation with substituted salicylaldehyde (salicylaldehyde, 5-nitrosalicylaldehyde or 4-(diethylamino)salicylaldehyde). The binuclear metal(II) complexes were prepared by the direct reaction of ligands (HL^{1-3}) with an equimolar amount of metal(II) nitrates in ethanol (**Scheme 1**). All the complexes were soluble in polar solvents like ethanol, DMSO and DMF. The elemental and spectral analyses agree well with the proposed structure of the complexes.

3.2. Crystal structure of ligand HL^3

The crystal structure of ligand HL^3 has been authenticated by single crystal X-ray diffraction method, which crystallizes in a monoclinic crystal system with $P2_1/n$ space group. The ORTEP diagram of ligand HL^3 with the atomic labeling scheme is shown in **Fig. 1** while a summary of crystallographic data collection and refinement parameters are compiled in **Table 1**. The selected bond lengths and bond angles are depicted in **Table S1**.

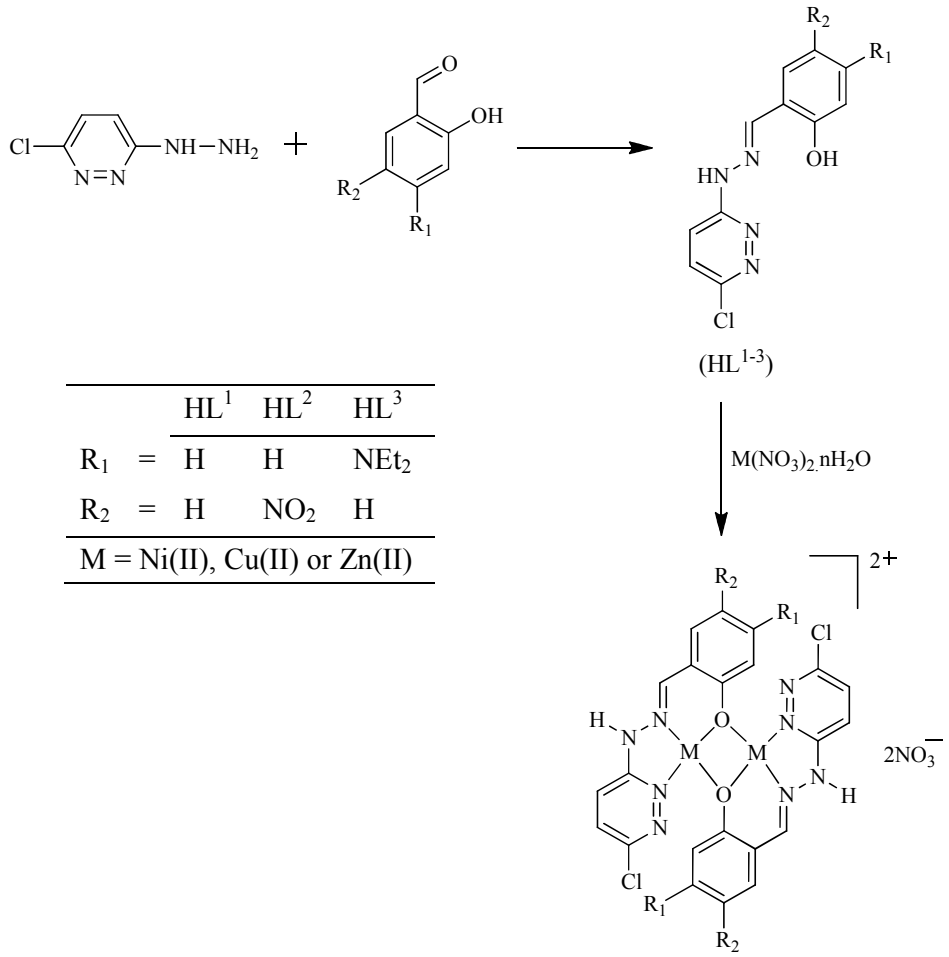

	HL[1]	HL[2]	HL[3]
R_1 =	H	H	NEt_2
R_2 =	H	NO_2	H
M = Ni(II), Cu(II) or Zn(II)			

Scheme 1 Schematic route for the synthesis of ligands (HL^{1-3}) and binuclear metal(II) complexes (**1-9**).

In the crystal structure, the chloro substituted pyridazine A (C1−C4/N4/N5/Cl1), the central part B (C5/N2/N3), the phenyl ring C (C6-C11), the two diethylamino group D (C12/C13/N1) and E (C14/C15/N1) are planar with root mean square (r.m.s) deviation of 0.0056, 0.0000, 0.0080, 0.0000 and 0.0000 Å, respectively. The dihedral angle between A/B, A/C and B/C are 10.08 (0.15)°, 14.55 (0.07)° and 5.89 (0.17)°, respectively, indicating that they are conjugated to allow extensive π overlap. The bond length of C5−C6 (1.445 (3) Å) is intermediate between single and double carbon-carbon bond while the bond lengths of C4−N3 (1.364(3) Å) and C9−N1 (1.389(3) Å) are intermediate between the single and double carbon-nitrogen bond, which indicates the partial delocalization of electron in the molecule.

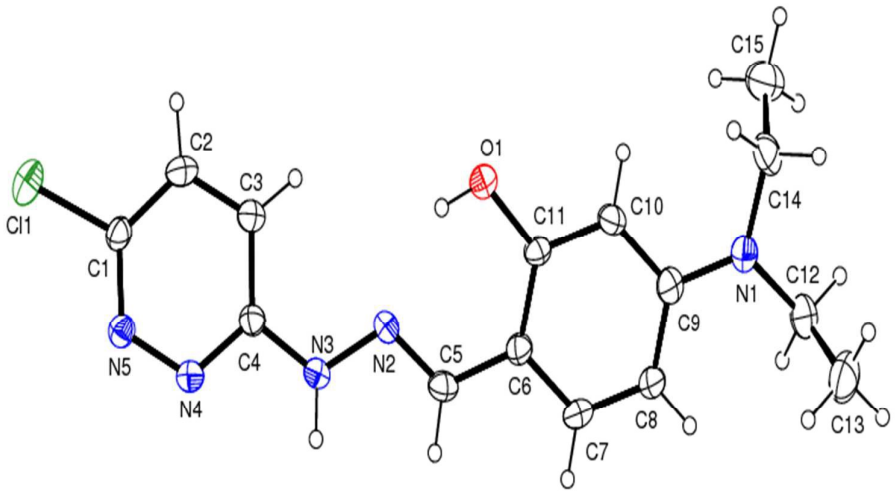

Fig. 1 The ORTEP diagram of the ligand HL^3 with the atomic numbering scheme.

The crystal lattice packing showing the internuclear hydrogen bonding is shown in **Fig 2**. The crystal packing diagram projecting along the crystallographic *b*-axis is depicted in **Fig. S1** and the hydrogen bonding parameters are shown in **Table S2.** The presence of ortho-hydroxyl group in Schiff bases favors the intramolecular hydrogen bonding. Two types of intramolecular hydrogen bonds, either O−H···N (enol-imine form) or N−H···O (keto-amine form) are possible in 2-hydroxy Schiff bases. The Schiff bases derived from salicylaldehyde always form the N−H···O type of hydrogen bonding, regardless of the nature of the *N*-substituent [33]. In the crystal structure of HL^3, the molecular conformation has been stabilized by intramolecular O1−H1···N2 hydrogen bond resulting in the formation of a six membered ring. This indicates that only enol–imine form has been favored than the keto form. These are evident from the observed C11−O1 bond distance of 1.361 Å, which is consistent with a single bond and the N2=C5 bond distance of 1.292 Å, which is indicative of a double bond. Each molecule of ligand HL^3 has three intermolecular hydrogen-bonding with bond length of 2.48, 2.67 and 2.054 Å.

Table 1 Crystal data and structure refinement details for ligand HL^3.

Empirical Formula	$C_{15}H_{18}N_5OCl$
Formula weight	319.79
Temperature (K)	293 (2)
Wavelength (Å)	0.71073
Crystal system	Monoclinic
Space group	*P21/n*
a (Å)	6.7997(5)
b (Å)	9.5387(8)
c (Å)	24.3565(19)
α (°)	90
β (°)	95.512(8)
γ (°)	90
Volume, V (Å^3)	1572.5(2)
Z	4
Density, ρ_{calc} (mg/m^3)	1.351
Absorption coefficient (mm^{-1})	0.252
F(000)	672
Crystal size (mm)	0.35 × 0.30 × 0.20
θ Range for data collection (°)	2.29 to 24.99
Limiting indices	$-8 \le h \le 7, -11 \le k \le 11, -28 \le l \le 28$
Reflections collected	22501
Independent reflections	22501 [R(int) = 0.0000]
Max. and min transmission	0.9593 and 0.9129
Refinement method	Full-matrix least-squares on F^2
Data/restraints/parameters	22501/2/205
Goodness of fit on F^2	1.085
Final R indices	R1 = 0.0873, wR2 = 0.1891
R indices (all data)	R1 = 0.1530, wR2 = 0.2150
Largest diff. peak and hole (e.Å^{-3})	0.341 and −0.409

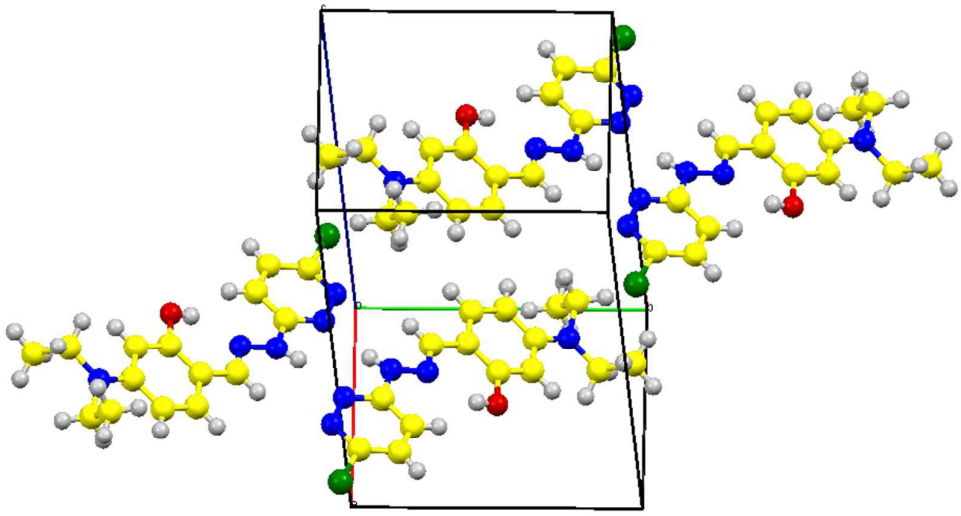

Fig. 2 View of crystal lattice packing showing the internuclear hydrogen bonding of ligand HL^3.

3.3. Spectral characterization

IR spectra provide valuable information regarding the mode of coordination of the ligand to the metal ion (**Table S3**). Coordination of the Schiff base ligands to the metal ions through the nitrogen atom is expected to reduce electron density in the azomethine link and lower the ν(C=N) absorption frequency [34]. The ν(C=N) stretching vibration (1628−1631 cm^{-1}) of azomethine group is shifted to lower wavenumber side (1601–1615 cm^{-1}) with a frequency difference Δν of 13–28 cm^{-1} indicating the involvement of azomethine nitrogen in coordination to the metal ion. Similarly, involvement of phenolic −OH group of ligands in bonding with the metal ions can be inferred from the appearance of ν(Ar−O) stretching vibration in the lower frequency (1240−1277 cm^{-1}) with respect to ligands (1283−1290 cm^{-1}) with a frequency difference Δν of 6–50 cm^{-1} [35]. The band assigned to ν(N=N) stretching vibration of the unsymmetrical pyridazine ring was located at 1518–1535 cm^{-1} for all the ligands, which was shifted to 1539–1568 cm^{-1} in the complexes suggesting the participation of the pyridazine nitrogen to the metal coordination. Appearance of new weak bands in the region 512–568 and 421–454 cm^{-1} in the spectra of all the complexes were assigned to the

stretching frequencies of ν(M−O) and ν(M−N) bonds, respectively [36]. The presence of anions is indicated by the typical stretching vibration of nitrate at 1380–1387 cm^{-1} for all the complexes. All these features were consistent with the proposed structure of the complexes indicating that all the ligands are coordinated to the central metal ion as monoanionic tridentate ligand through a nitrogen atom of the azomethine group, one of the nitrogen atom of the pyridazine ring and an oxygen atom of the phenolic group.

The formation of ligands (HL^{1-3}) was further authenticated by ^{1}H, ^{13}C and ^{13}C DEPT-135 NMR spectra (**Fig. S2-S10**). The main chemical shifts of the proton signals in the ^{1}H NMR spectra and related chemical shifts of the carbon signals in ^{13}C NMR of the ligands (HL^{1-3}) with their assignments are listed in **Table S4**. ^{1}H NMR spectroscopy provided evidence for the monosubstitution as the singlet assignable to the equivalent aromatic protons of the 3,6-dichloropyridazine (starting material) at 7.51 ppm splits into two doublets at 7.45 and 7.11 ppm, while the primary amine (NH_2) and secondary amine (NH) protons appears at 4.40 and 8.23 ppm, respectively in the ^{1}H NMR spectrum of 3-chloro-6-hydrazinopyridazine. After condensation of 3-chloro-6-hydrazinopyridazine with appropriate salicylaldehyde, the ligands (HL^{1-3}) formed were confirmed by the imine formation evidenced by a signal around 8.50–8.23 ppm. The primary amine peak at 4.40 ppm was disappeared and the secondary amine peak was shifted downfield to 11.60–10.17 ppm. A signal around 11.80−11.27 ppm indicates the presence of phenolic hydroxyl group, which was shifted downfield because of the intramolecular hydrogen bonding between it and the azomethine nitrogen. The peaks corresponding to the aromatic proton were observed in the region 6.89–8.04 ppm. The presence of diethylamino substituent in the ligand HL^{3} is evidenced by a quartet peak at 3.36 ppm corresponding to four methylene hydrogens and a triplet peak at 1.18 ppm due to six methyl hydrogens.

The ^{13}C NMR spectra of the ligands (HL^{1-3}) were characterized by the presence of characteristic signals at 143–137 ppm for the azomethine carbon (C=N). The spectra were further characterized by the absence of the CHO proton signal at 190 ppm from the corresponding aldehydes and the carbons of phenyl ring were observed in the range of 130–104 ppm. The peaks corresponding to methylene and methyl carbons for the ligand HL^3 were observed at 44 and 13 ppm, respectively. The ^{13}C NMR signals of the synthesized ligands have further been substantiated by ^{13}C DEPT-135 spectra (Distortionless Enhancement by Polarization Transfer), a technique for ^{1}H-decoupled-^{13}C spectra used as a means of enhancing signal intensity, which can show positive CH_3 and CH, and negative CH_2 signals while non-proton-bearing carbons are not seen in DEPT spectra because the technique relies on polarization transfer. The DEPT-135 spectra exhibited signals for azomethine carbon of the Schiff bases (HL^{1-3}) in the range of 143-137 ppm. The quaternary carbon atom signals seen in the ^{13}C NMR spectra for the ligands (HL^{1-3}) have been disappeared in DEPT-135. The DEPT-135 spectra of ligand HL^3 shows a negative signal for methylene carbon at 44 ppm. Hence, the formation of the ligands (HL^{1-3}) has been clearly authenticated by the NMR spectroscopy.

The ESI mass spectra provide additional structural information about the stereochemistry of the studied complexes, which was characterized by moderate to high relative intensity molecular ion peaks. The observed molecular ion peaks for the binuclear complexes were consistent with the proposed empirical molecular formulae. **Fig. 3** shows the ESI mass spectra of complexes **4** and **5,** which show a molecular ion (M^+) peak at *m/z* = 620.93 and 710.90, respectively, suggesting that the complexes are binuclear in nature. They also exhibit an additional peak at *m/z* = 622.92 and 712.89, respectively, corresponds to (M+2) peak attributed to the isotope peaks due to ^{37}Cl. The base peaks at *m/z* = 309.96 and 354.95 for the complexes **4** and **5** are due to $[CuL^1]^+$ and $[CuL^2]^+$, respectively.

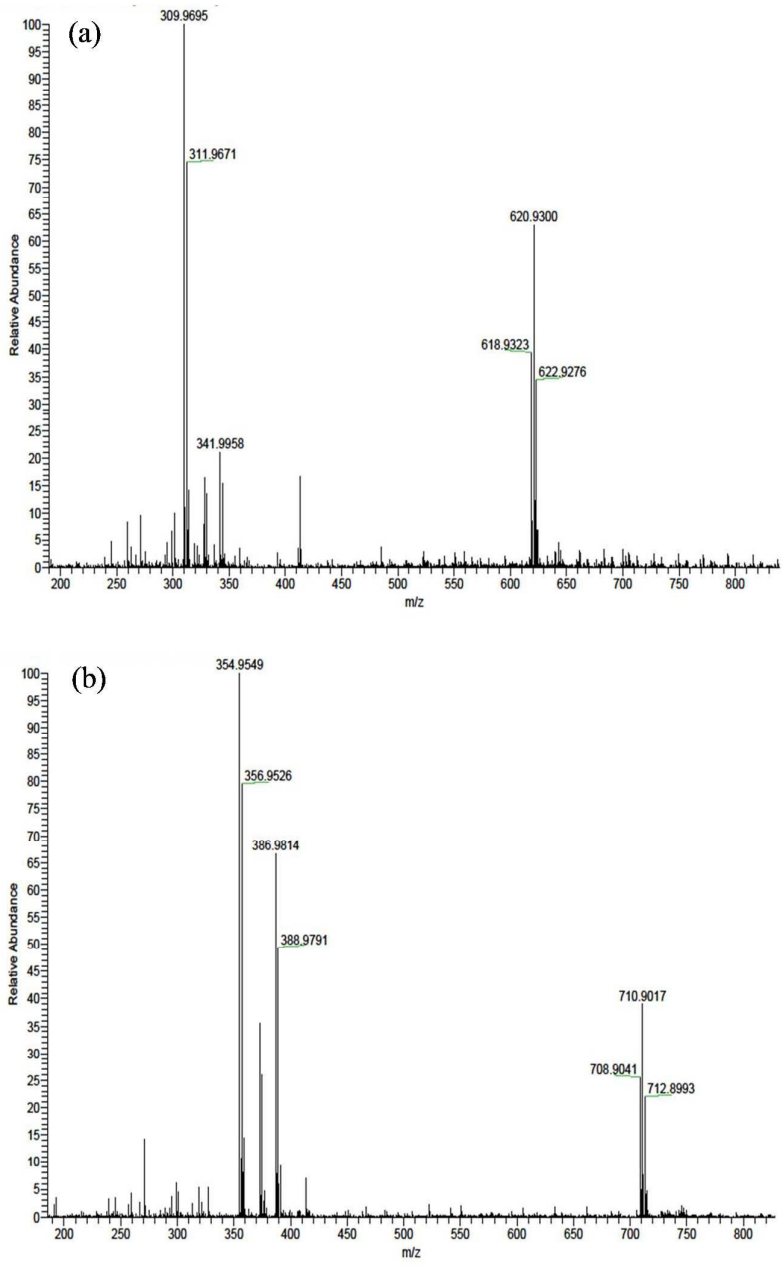

Fig. 3 ESI-mass spectra of the copper(II) complexes **4** (a) and **5** (b).

The electronic spectra of the ligands (HL^{1-3}) and metal(II) complexes (**1-9**) were recorded in DMSO in the range of 200-800 nm (**Fig. S11-S13**), and the data are presented in **Table S5**. The ligands $HL^{1\&3}$ exhibit a single absorption peak at 336 and 371 nm respectively attributed to π-π* intra-ligand transition whereas the ligand HL^{2} exhibits peaks at 336 and 465 nm assigned to π-π* and n-π* intra-ligand transitions, respectively. The high hyperchromic

shift exhibited by the ligand HL^3 when compared to ligands $HL^{1\&2}$ may be due to the presence of electron-releasing $-N(Et)_2$ group in the ligand HL^3. The metal(II) complexes show less intense π-π* intra-ligand transition than their respective free ligands with considerable blue shift except for zinc(II) complexes. The binuclear nickel(II) complexes (**1-3**) exhibit LMCT band at 412−423 nm and a weak d-d band around 572–594 nm due to $^2A_{1g} \rightarrow {}^2A_{1g}$, which suggest square planar geometry for the complexes [37]. The electronic spectra of copper(II) complexes (**4-6**) show an intense ligand to metal charge transfer transition around 411−441 nm and the d-d band in the range 611–655 nm which can be assigned to $^2B_{1g} \rightarrow {}^2A_{1g}$ transition suggesting a square planar geometry [38]. The zinc(II) complexes (**7-9**) exhibit a single peak at 319−338 nm due to π-π* intra-ligand transition and no d-d transition was observed for these complexes due to the lack of metal to ligand charge transfer transition because of d^{10} electronic configuration of zinc(II) complexes, and tetrahedral geometry is assigned for these complexes.

The emission properties of the ligands (HL^{1-3}) and metal(II) complexes (**1-9**) were studied at room temperature in 1×10^{-5} M DMSO (**Fig. 4, 5 & S14**) and the data are presented in **Table S6**. The process such as magnetic perturbation, redox activity, electronic energy transfer etc., may quench the fluorescence of a ligand by transition metal ions during complexation. However, enhancement of fluorescence through complexation is much of interest due to the photochemical applications of these complexes [39, 40].

The ligands HL^{1-3} exhibit the photoluminescence with weak intense emission at 415, 439 and 481 nm, respectively. However, the nickel(II) complexes **1** and **2** show an intense broad band at 341 and 473 nm, respectively, and the copper(II) complexes **4** and **5** exhibit an intense band at 331 and 346 nm, respectively whereas the zinc(II) complexes **7** and **8** exhibit intense band at 395 and 322 nm, respectively. These emissions are neither metal-to-ligand charge transfer (MLCT) nor ligand-to-metal charge transfer (LMCT), but they may be

assigned to intra-ligand (n-π* or π-π*) fluorescence. However, the factor of chelation induced rigidity also plays an important role in causing a change in the fluorescence behavior of the free ligand on complexation with the metal ions. The rigidity induced in the complexes is in turn dependent on the coordination geometry that the ligand assumes around the metal center [41]. The Schiff bases synthesized here have imine moiety, which exhibits poor fluorescence in part due to isomerization of the C=N double bond in the excited state and in part due to excited-state proton transfer (ESPT) involving the phenolic protons. Upon stable chelation with metal ions, the C=N isomerization was inhibited; additionally, the coordination of the ligands with the respective metal(II) ions prevents ESPT, leading to fluorescence enhancement. Moreover, the reaction of a metal ion with a chelating agent induces rigidity in the resulting molecule and tends to produce a large chelation-enhanced fluorescence effect (CHEF), which induces the large enhancement of fluorescence intensity [42]. Hence, these Schiff bases ligands (HL^{1-3}) may also be used as a fluorescent probes for metal ions.

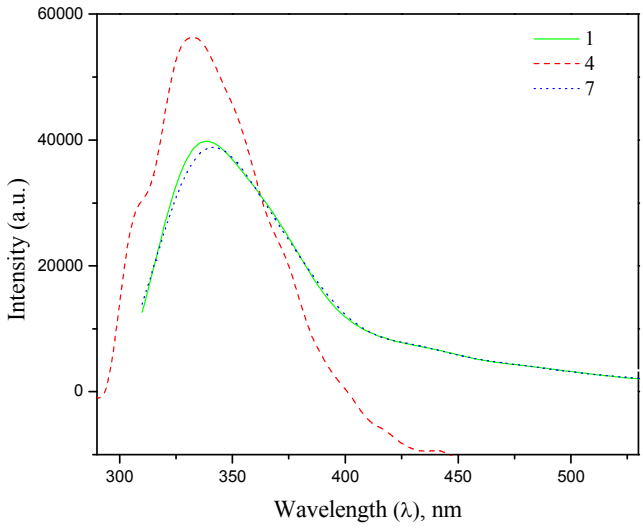

Fig. 4 Photoluminescence (PL) spectra of binuclear metal(II) complexes (**1, 4** & **7**) of ligand HL^1.

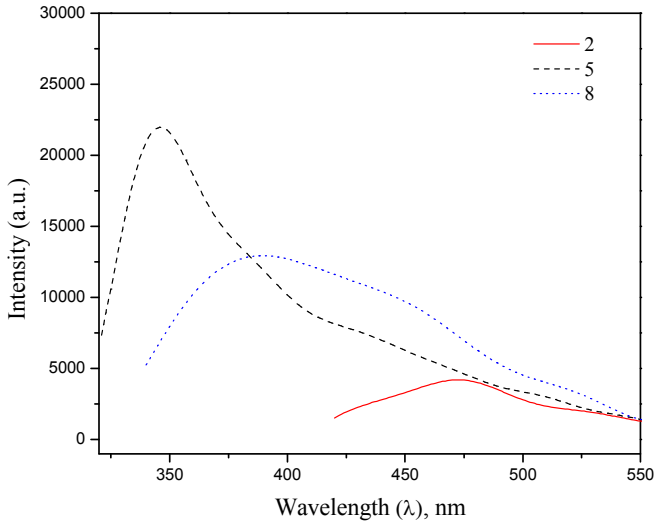

Fig. 5 Photoluminescence (PL) spectra of binuclear metal(II) complexes (**2, 5** & **8**) of ligand HL^2.

EPR studies of polycrystalline samples were recorded at room temperature (**Fig. 6**). The $g_{\|}$ and $g_{\perp}$ values for the copper(II) complexes (**4-6)** have been calculated as 2.249−2.262 and 2.058−2.092, respectively, while the g_{av} value was determined to be 2.121−2.146 from the relation $g_{av} = (g_{\|} + 2g_{\perp})/3$. These calculated data are in agreement with an orbitally non degenerate state for the four-coordinate copper(II) complexes under investigation. According to Hathaway *et al.* [43] axial symmetry parameter G, determined as $G = (g_{\|}-2.0023)/(g_{\perp}-2.0023)$, measures the exchange interaction between the metal centers in a polycrystalline solid. If G > 4, the exchange interaction is negligible, but if G < 4 indicates considerable exchange interaction in the solid complexes. The copper(II) complexes have G values lesser than 4 indicating the presence of exchange interaction in the solid complexes. The value of $g_{\|} > g_{\perp} > 2.0023$ and G value within the range 2.5–4.0 are consistent with a $d_{x^2-y^2}$ ground state, and a square based geometry can be proposed for the complexes [44]. The $g_{\|}$ value, a moderately sensitive function is used for the indication of covalency. The $g_{\|} > 2.3$ is characteristics of an ionic environment and $g_{\|} < 2.3$ is of covalent environment in M−L

bonding [45]. The observed $g_{\|}$ values for the complexes was less than 2.3, in agreement with the covalent character of the M−L bond which has been further supported by the G value, which was less than 4.0 [46].

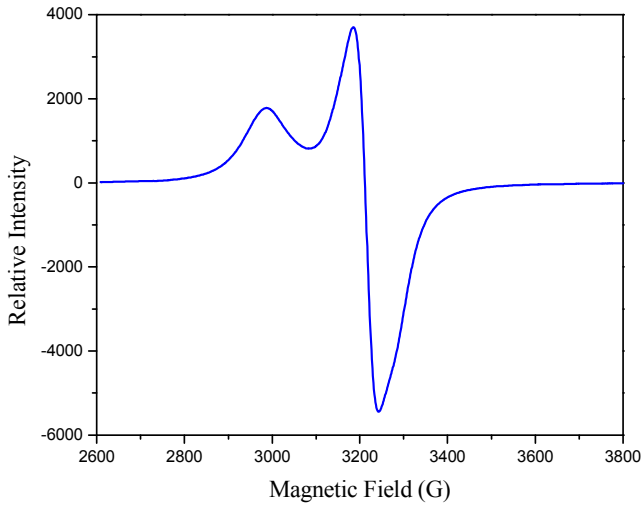

Fig. 6 EPR spectrum of the copper(II) complex **4**.

The magnetic moment values of binuclear copper(II) complexes (**4-6**) at room temperature was found in the range of 1.59-1.63 B.M, which is below the 'spin only' value of 1.73 B.M. The lower value of magnetic moment at room temperature is consistent with square planar geometry around the metal ions and are attributed to the anti-ferromagnetic exchange interaction between two copper(II) metal ions, which indicates the formation of binuclear complexes [47].

3.4. Electrochemical properties

The conductivity measurements in non-aqueous solutions can be used in structural studies of metal complexes within the limits of their solubility and provide a method of testing the degree of ionization of the complexes. The molar conductivity values in DMF solution (10^{-3} M) at 25 °C for all the complexes were in the range 131–172 $\Omega^{-1}cm^2mol^{-1}$ indicating 1:2 electrolytic behavior [48], implying the non-coordination of nitrate anions to the central metal(II) ion.

3.4.1. Reduction process at cathodic potential

The redox properties of the binuclear nickel(II) and copper (II) complexes (**1-6**) were studied by cyclic voltammetry in the range 0 to –1.2 V in DMF using TBAP as the supporting electrolyte (**Fig. S15**) and the data are summarized in **Table S7**. The binuclear complexes in the cathodic region display two step irreversible one electron transfer reduction process. The first reduction wave appeared in the potential range ($^1E_{pc}$) −0.323 to −0.463 V while the second reduction potential ($^2E_{pc}$) was observed at −0.634 to −0.790 V, which can be attributed to the redox couple species generally as:

$$M_2^{II} \rightarrow M^{I}M^{II} \rightarrow M_2^{I}$$

3.4.2. Oxidation process at anodic potential

The cyclic voltammograms of binuclear nickel(II) complexes (**1-3**) in the anodic region are shown in **Fig. S16** and the data are summarized in **Table S7**. In the anodic potential region, the nickel(II) complexes show two step irreversible one electron oxidation process. The first oxidation wave was obtained in the range from +1.009 V to +1.024 V, while the second oxidation wave obtained in the region from +1.140 V to +1.153 V. The two oxidation processes for the nickel(II) complexes were assigned as follows:

$$Ni_2^{II} \rightarrow Ni^{III}Ni^{II} \rightarrow Ni_2^{III}$$

3.5. Computational details

3.5.1. Geometry optimization

In the absence of crystal data, it was thought worthwhile to obtain structural information through molecular modeling. Molecular mechanics, which provides the energy minimized conformation is a tool of increasing importance for the structural investigation of coordination and organometallic compounds. Complexes **1**, **3**, **5** and **9** were optimized at B3LYP/LANL2DZ and B3LYP/GEN levels in the gas phase. The optimized ground state geometry structures of these complexes are shown in **Fig. S17,** and the calculated structural

parameters (bond lengths and bond angles) are given in **Table S8** along with the reported experimental values [14, 38]. The acceptable results were obtained by DFT/B3LYP method with LANL2DZ and GEN basis sets for the complexes **1**, **3**, **5** and **9**. The calculated values of bond angles obtained by using B3LYP/LANL2DZ level are more appropriate than the B3LYP/GEN level. Therefore, DFT/B3LYP/LANL2DZ level was preferred to B3LYP/GEN level for determining the molecular structure. The B3LYP method in combination with the LANL2DZ basis gives an excellent estimation of M–N bond distances, M–N2, M–N4, M–O1, M–O2, M–N7 and M–N9. Molecular geometries can be predicted by calculating τ values from the following equation [49]:

$$\tau = \frac{\beta - \alpha}{60}$$

where α and β are the equatorial and axial bond angles, respectively. Generally, if the molecular geometry is square planar, τ value is close to 0, while the τ value close to 1 indicates tetrahedral geometry. If τ value is between 0 and 0.5, the molecular geometry is distorted tetrahedral. For the complex **9**, α (N(2)−Zn(1)−N(4)) value is 79.64° and β (N(9)−Zn(1)−O(1)) value is 88.39°. For complexes **1**, **3** and **5** α (N(2)−Ni(1)−N(4)), (N(2)−Ni(1)−N(4)) and (N(2)−Cu(1)−N(4)) values are 78.00°, 77.47° and 78.88°, respectively and β (N(9)−Ni(1)−O(1)), (N(9)−Ni(1)−O(1)) and (N(9)−Cu(1)−O(1)) values are 84.02°, 83.09° and 84.15°, respectively. Based on the above results, distorted tetrahedral geometry is adopted by the complex **9** as their τ values lies between 0 and 0.5. In the case of complexes **1**, **3** and **5**, the value of τ is equal to 0, which indicate the square planar geometry for the nickel(II) and copper(II) centers. Generally, the calculated bond lengths are longer than the experimental data because the former are optimized in the gas phase and the latter are in a tight crystal lattice. The calculated bond lengths and bond angles agree reasonably with the reported experimental values.

3.5.2. Frontier molecular orbital (FMO) analysis

FMOs (HOMO and LUMO) play an important role in the study of electrical and optical properties. Additionally, the HOMO-LUMO energy gap values help to exemplify the chemical reactivity, kinetic stability and electrical transport properties of the molecule [50]. Recently, the HOMO-LUMO energy gap has been used to prove the bioactivity from intramolecular charge transfer and this energy gap values also correlated with various biological systems like antibacterial, antioxidant and DNA binding studies [51−53]. A variety of applications are available for the use of the HOMO-LUMO gap as a quantum descriptor in establishing correlation in various chemical and biochemical systems [54, 55]. Molecules with a lower HOMO-LUMO energy gap show a noteworthy degree of intramolecular charge transfer (ICT) from the electron-donor groups to the electron-accepter groups through π-conjugated path [56]. This explains the extent of ICT from the electron-donor groups to electron-acceptor groups through conjugated path. A large HOMO-LUMO gap implies high stability for the molecule in the sense of its lower reactivity in chemical reactions [55]. Systems having high E_{HOMO} are good electron donors while those having low E_{LUMO} energy are good electron acceptors. The orbital energy level analysis for complexes **3**, **5**, **6**, **7** and **9** showed that E_{HOMO} values are –2.49, –1.76, –2.47, –2.21 and –2.56 eV, respectively while E_{LUMO} values are −1.54, –0.34, –1.24, –0.86 and –1.91 eV, respectively. As a result, complexes **3**, **6,** **7** and **9** are better electron donors while complex **5** is a better electron acceptor. The ΔE values of complexes **3** (0.95 eV), **5** (1.42 eV), **6** (1.23 eV), **7** (1.35 eV) and **9** (0.65 eV) calculated at the DFT level reflects the higher stability of **3** and **9** compared to other complexes (**Fig. 7** & **S18**). It could be noted that **3** and **9** has higher ability towards the intramolecular charge transfer than the other complexes. The energy gap value indicates the

eventual charge transfer interactions within the molecule, and also the obtained lower band gap value supports the observed trend of biological activity.

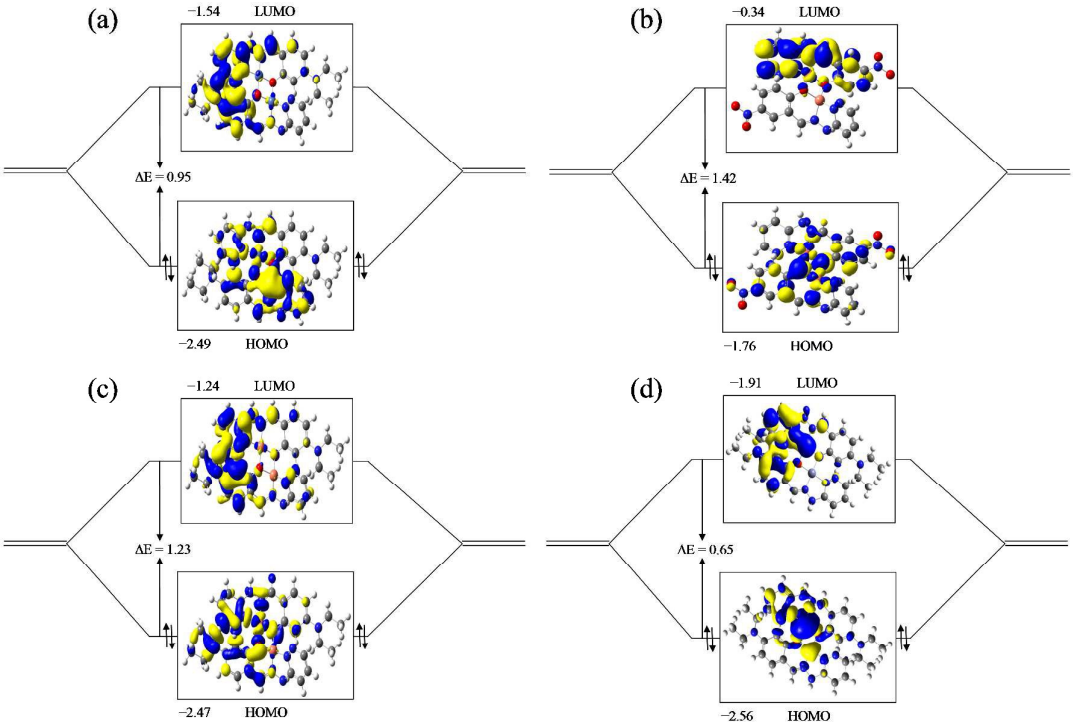

Fig. 7 Frontier molecular orbitals of the complexes **3** (a), **5** (b), **6** (c) and **9** (d).

Generally, the electronic properties of the molecules are calculated from the total energies and the Koopman's theorem. In this context, ionization potential was calculated from IP = $-E_{HOMO}$ while the electron affinity is computed from EA = $-E_{LUMO}$. Further, important quantities such as electronegativity (χ), hardness (η), softness (ζ), and electrophilicity index (ψ) were deduced from ionization potential and electron affinity values.

Electronegativity (χ) $\mu = -X = \dfrac{IP + EA}{2}$

Chemical hardness (η) $= \dfrac{IP - EA}{2}$

Softness (ζ) $= \dfrac{1}{2\eta}$

Electrophilicity index (ψ) $= \dfrac{\mu^2}{2\eta}$

The obtained values of electronegativity, chemical hardness, softness, and electrophilicity index are 2.01, 0.47, 1.06 and 4.29 eV for complex **3** and 2.23, 0.32, 1.56 and 7.77 eV for complex **9**, respectively. The energy gap and softness values indicate that the complexes **3** and **9** show high chemical reactivity when compared to other complexes.

3.6. Anticancer activity

3.6.1. Cell viability assay

A chemical entity is said to be an anti-cancer agent when it selectively kills cancer cells without causing excessive damage to normal cells [57]. The anticancer effect of complexes in normal (rat myoblast L-6 cells) as well as cancer cells (human breast cancer MDA-MB-231 cells) was assessed by MTT assay. The IC_{50} values for all the complexes in both the cell lines are given in **Table 2**. The values are obtained by non-linear fitting of log dose-response curve (**Fig. S19** & **S20**) using the GraphPad Prism software. IC_{50} value represents the concentration required to achieve the 50% of cell viability when compared to control. Complexes with lower IC_{50} value are more potent than those with higher IC_{50} value.

The complexes **1**, **4** and **6** are the potent anticancer agent as they have low IC_{50} values, but there is no difference in IC_{50} values between normal and cancer cells, which make them unsuitable candidates as anti-cancer agent. Even though there is significant difference in IC_{50} values between normal and cancer cells for complexes **5** and **7**, the values are too high to qualify them as anti-cancer candidate. The complexes **2**, **3** and **9** exhibit low IC_{50} values against cancer cells and they are relatively less toxic to normal cells, and it must be noted that these complexes on the normal cell lines (L-9) displayed lower cytotoxicity than that of them against the tested cancer cell line (MDA-MB-231), thereby exhibiting selectivity to these cancer cells. The structure of complexes **3** and **9** is very similar except their metal centers. Complexes **3** and **9** due to the synergistic effect of the ligand HL^3 with the metal ions exhibited higher anticancer activity than the free HL^3 ligand and their corresponding metal

nitrate salts against MDA-MB-231 cell line. The proliferation-inhibitory activity of complexes **3** and **9** on the human breast cancer cell line (MDA-MB-231) is higher than that of the standard drug cisplatin. Hence, these complexes were used as a representative compounds to carry out the clonogenic assay, apoptotic and cell cycle analysis on MDA-MB-231 cancer cell line.

Table 2 IC_{50} values for complexes (**1-9**) and cis-platin against MDA-MB-231 and L-6 cell lines using MTT assay.

Complexes	IC_{50} (in μM)	
	MDA-MB-231	L-6
1	0.36	0.40
2	59.29	67.48
3	74.65	94.63
4	0.34	0.36
5	306.2	386.1
6	12.0	14.17
7	512.5	741.2
8	462.1	470.0
9	36.48	47.27
Cis-platin	91.28	–

3.6.2. Cell clonogenic assay

The antiproliferative effects of complexes **3** and **9** on MDA-MB-231 cells were confirmed from the colony-formation to measure clonogenic survival. The ability of a cell to form a colony (minimum 50 cells) is detemined by cell clonogenic assay. Such cells gain ability to proliferate indefinitely. It is clear from the **Fig. 8** that the treatment of colonies with both the complexes resulted in decrease in number and size of colonies when compared with untreated controls, which causes cells to loose their reproducive integrity and the complexes inhibit the growth and proliferative of MDA-MB-231 cells.

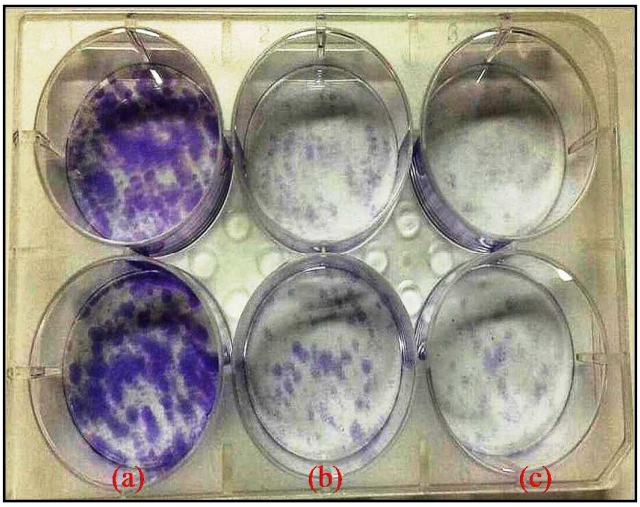

Fig. 8 Clonogenic assay for MDA-MB-231 cells treated with 0.1% DMSO (control) (a), complexes **3** (b) and **9** (c). Colonies of cells were treated with 0.1% DMSO, IC_{50} concentrations of complexes **3** and **9** for 24 h and then incubated for a week followed by staining with crystal violet.

3.6.3. Apoptotic studies by AO/EB fluorescent staining

Apoptosis is a normal component of the development and maintenance of health of multicellular organisms. Cells die in response to a variety of external and physiological stimuli. During apoptosis, the cell death is in a controlled and regulated fashion, which makes it different from the other forms of cell death called necrosis in which uncontrolled cell death leads to cells lysis, to inflammatory responses, and potentially to serious cell problems. Most tumour cells retain their sensitivity to some apoptotic stimuli from chemotherapeutic agents and in this context the apoptosis-inducing ability of drugs seems to be a primary factor in determining their efficacy [58]. Therefore, the mode of cell death induced by the complexes **3** and **9** have been studied using dual AO/EB fluorescent staining visualized under a fluorescent microscope, which can be used to identify apoptosis-associated changes in cells. Ethidium bromide (EB) intercalates DNA double helix and acridine orange (AO) forms complexes with either double-stranded DNA or single-stranded DNA and RNA. Live cells appear to have normal nuclei staining, which present green chromatin with organized structures, apoptotic cells contain condensed or fragmented chromatin (orange) and necrotic cells have normal

nuclei staining as live cells except the chromatin is orange. The percentage of apoptotic and necrotic cells were calculated. Control sample showed green nuclei with organized structure indicating live cells whereas treated samples showed fragmented chromatin (**Fig. 9**). The treatment did not cause necrosis of cells. The treatment of cells with 75 μM of complex **3** resulted in 44% apoptotic cells while with 37 μM of complex **9** resulted in 51% apoptotic cells. The data shows that both the complexes cause cytotoxicity in MDA-MB-231 cells *via* apoptotic pathway.

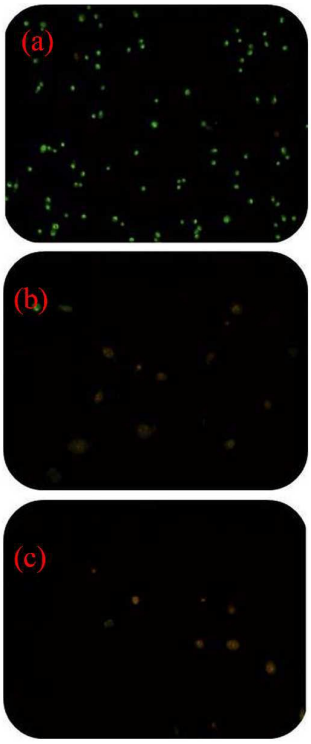

Fig. 9 Analysis of apoptotic inducing effect on MDA-MB-231 cells for 24 h with 0.1% DMSO (control) (a), complexes **3** (b) and **9** (c) with the IC_{50} concentrations followed by AO/EB staining and observed under fluorescence microscope.

3.6.4. Cell cycle analysis

The effect of treatment of complexes **3** and **9** at IC_{50} concentrations on cell cycle distribution against MBA-MB-231 cells was checked using flow cytometry for 24 h. The treatment caused changes in cell size distribution as seen in **Fig. 10a**. The results indicate that

the complexes **3** and **9** caused an increase in the number of cells in S phase and sub G0 phase of the cell cycle (**Fig. 10b**).

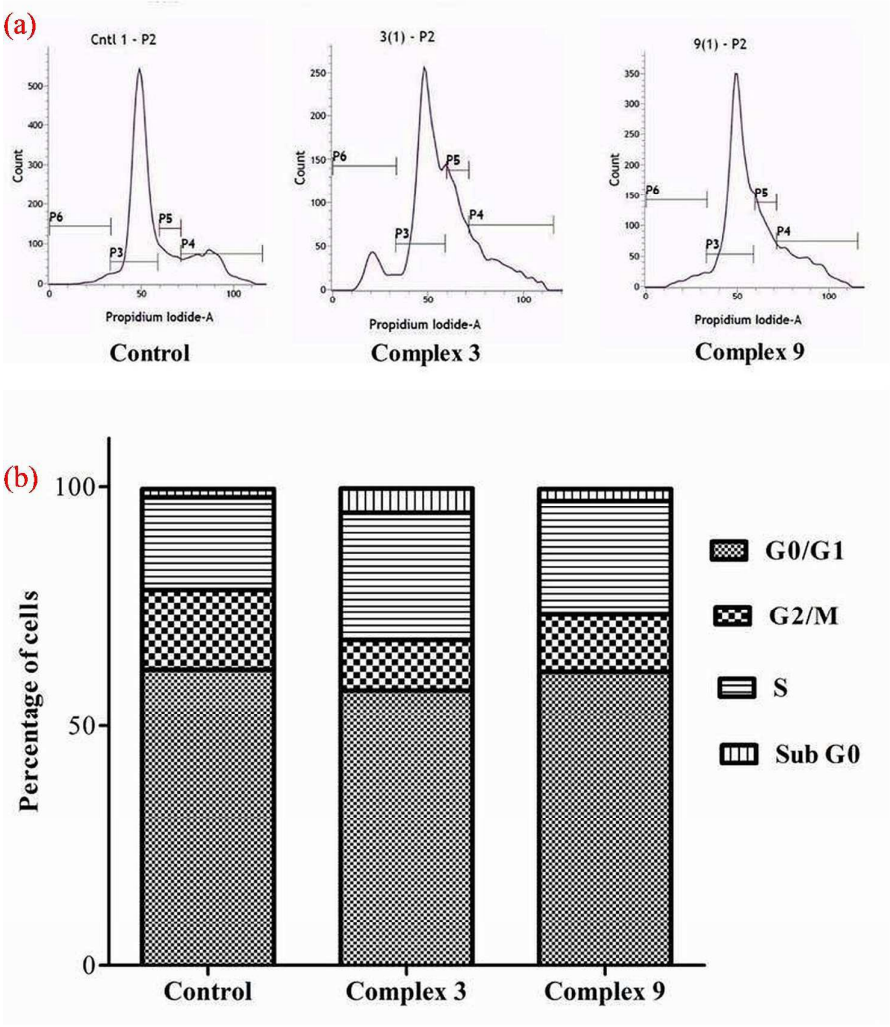

Fig. 10 Cell cycle analysis of MDA-MB-231 cells after treatment with 0.1% DMSO (control), complexes **3** and **9** with the IC_{50} concentrations. (a) Distibution of cells in various phases of cell cycle. P3: G0/G1, P4: G2/M, P5: S and P6: Sub G0 phase of cell cycle. (b) Graphical representation of cells in various phases of cell cycle after treatment with complexes **3** and **9**.

The increase in proportion of the cells in S phase for complex **3** was observed from 19.4% to 26.5% whereas that with complex **9** was 23.8%. There are two reasons for the increase in percentage of cells in S phase. It could be because of an increase in the proliferation of cells or cell arrest in S phase due to DNA damage. The possibility of increased proliferation is ruled out as the concentration used reduces cell viability to 50% as

shown in MTT assay. So the complexes **3** and **9** induces apoptosis in cells by causing DNA damage, which causes arrrest of cells in S phase. Similar observation has been reported earlier for complexes to cause inhibition of cell cycle progression in the S phase [59].

3.7. Targeting of epidermal growth factor receptor (EGFR)

The epidermal growth factor receptor (EGFR) belongs to the receptor tyrosine kinase family, which is over expressed in a number of solid tumors [60]. Activation of the epidermal growth factor receptor by a number of ligands induces downstream signaling that modulates critical cell functions including growth, survival and differentiation. Abnormal epidermal growth factor receptor expression and activation is also involved in a number of cancers. Additionally, dimerization, oligomerization, and clustering of receptor molecules in the plasma membrane are now recognized as important factors in the control of signaling processes. A good example is the epidermal growth factor receptor (EGFR), one of a family of four receptors that initiate signaling cascades responsible for cell proliferation, motility, and survival [61]. In addition to its cognate ligands, the epidermal growth factor receptor can be activated by metals such as copper and zinc. Due to the important role of these metals in a number of diseases including neurodegenerative disorders, therapeutic approaches are being developed based on the use of lipid permeable metal-complexing molecules. While these agents are showing promising results in animal models and clinical trials, little is known about the effects of metal-ligand complexes on cell signaling pathways.

In order to study the binding site selection, complexes **3** and **9** were docked into the 3D structure (PDB ID: 1M17) of EGFR using AutoDock, and the docking results were listed in **Table 3.** The predicted active sites consisted of amino acids such as Leu694, Gly695, Val702, Lys721, Pro770, Phe771, Gly772, Cyc773, Leu774, Leu775, Asp776, Tyr777, Leu790, Trp793, Cyc794, Val795, Ile797, Met801, Leu814, Ala815, Ala816, Arg817, Asn818, Val819, Leu820, Ile829, Thr830, Asp831, Asp872, Ser875, Tyr876, Thr879,

Val880, Glu882, Leu883 and Phe937. **Fig. 11** provides more information concerning the energetically favorable docked images, the binding sites and the binding poses of the two complexes. It can be seen that both complexes most likely binds to the hydrophobic pocket, it is noteworthy that the complexes can interact with the active binding site of EGFR, especially charge interaction as well as hydrogen bonding with N−H and O−H of Ala816, Trp793 and Cys773, and it is in close proximity to hydrophobic residues such as Leu694, Gly695, Val702, Lys721, Tyr777, Met801, Leu814, Arg817, Leu820, Ile829, Thr830, Asp831 Asp872, Ser875, Glu882 and Phe937 of subdomain IIA of EGFR suggesting the existence of hydrophobic interaction between them. Both the complexes show π-π interaction between phenyl ring and amino group of Ala816, and methyl group of diethylamino substituent with amino acid Trp793 (**Fig. S21**). Comparing the binding affinity of both complexes, it can be seen that the binding strength of complex **9** to EGFR is higher than the complex **3**. The lower relative binding energy indicates the binding affinity between the EGFR and the target molecules to be more potent. Hence, the more negative relative binding energy of complex **9** indicate its stronger binding affinity to the EGFR than the complex **3**, because it contain a large hydrophobic cavity in the subdomain IIA, which play a key role in metabolism and transportation of EGFR. The obtained results from the molecular docking studies indicate that the interaction between the complexes and EGFR was dominated by hydrophobic forces, strong hydrogen bonding and π-π interactions. Also, these results suggest that the complexes can be stored and released by protein EGFR, which are significant for the further exploration of protein interaction of these complexes.

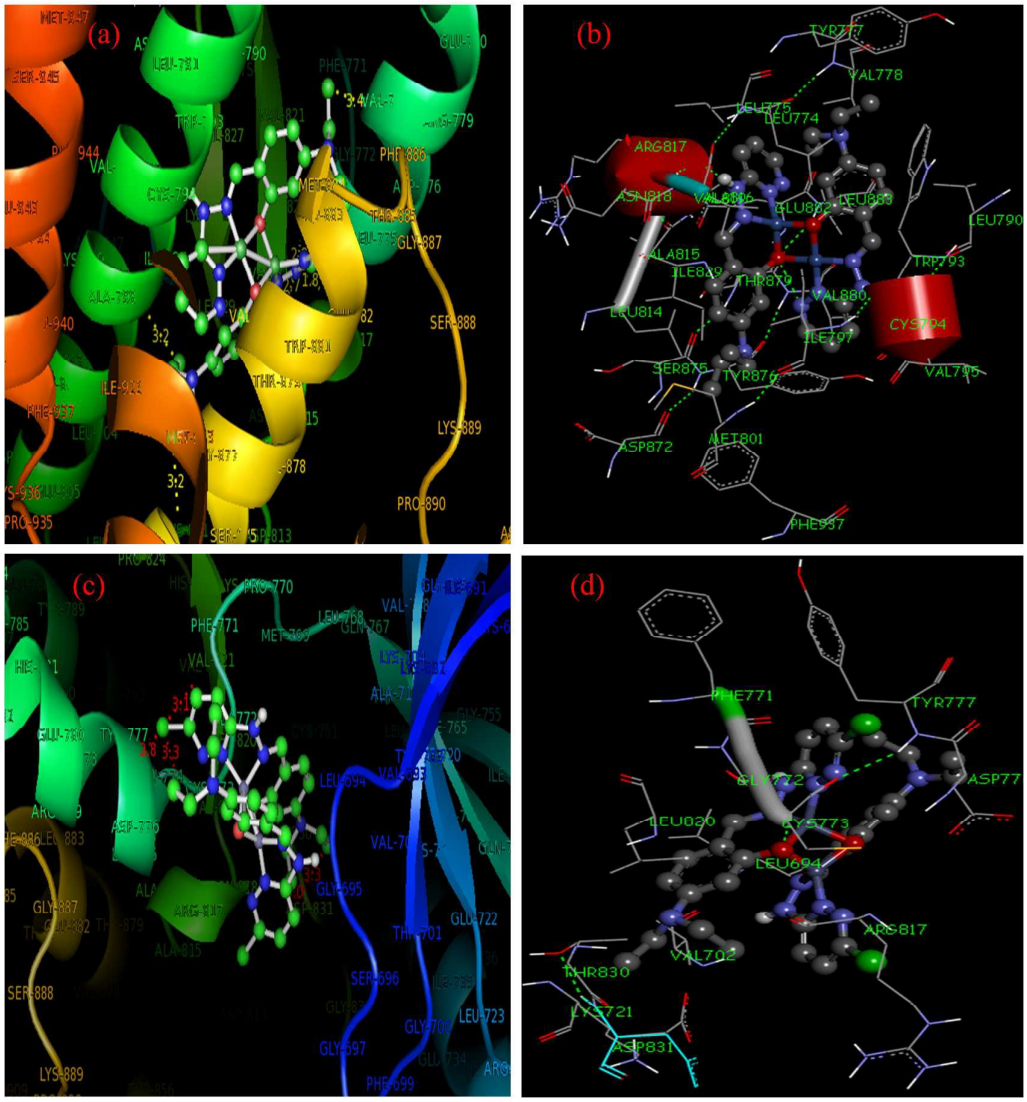

Fig. 11 Molecular docked model of the complex **3** located within the hydrophobic pocket of EGFR (a), the interaction mode between **3** and EGFR (b). Molecular docked model of the complex **9** located within the hydrophobic pocket of EGFR (c), the interaction mode between **9** and EGFR (d).

Table 3 Protein EGFR docking results of the binuclear complexes **3** and **9** (kcal mol^{-1}).

Complexes	vdW + H bond + dissolving energy ($\Delta G_{vdW+hb+desolv}$)	Electrostatic energy (ΔG_{elec})	Total internal energy (ΔG_{total})	Torsional free energy (ΔG_{tor})	Unbound system's energy (ΔG_{unb})	Binding free energy ($\Delta G_{binding}$)[a]
3	−7.86	−0.18	−0.82	1.34	−0.42	−7.10
9	−9.02	−0.20	−0.83	1.65	−0.55	−7.86

[a] $\Delta G_{binding} = \Delta G_{vdW+hb+desolv} + \Delta G_{elec} + \Delta G_{total} + \Delta G_{tor} + \Delta G_{unb}$.

4. Conclusion

Nine binuclear nickel(II), copper(II) and zinc(II) complexes derived from three tridentate pyridazine-based ligands have been synthesized and characterized on the basis of spectroscopic studies. The molecular structure of the ligand HL^3 has been studied using single crystal XRD. Electronic spectral data and magnetic moment measurement supports the square planar geometry for nickel and copper complexes while zinc complexes are assigned with tetrahedral geometry. The two complexes **3** and **9** have been found to exhibit higher *in vitro* cytotoxicity towards MDA-MB-231 cell lines with respect to their IC_{50} values determined by MTT assay. The cell cycle analysis indicates that the two complexes exhibit effective cell growth inhibition by triggering S phase. These cytotoxicity results suggest that the complexes **3** and **9** can be introduced as an effective metal-based anticancer drug. *In vivo* experiments in relevance to anticancer activity of these complexes can be considered for future studies.

Acknowledgments

The authors are grateful to Sophisticated Analytical Instruments Facility (SAIF), Indian Institute Technology Madras (IIT-M), Chennai 600 036, for single crystal XRD studies and Central Leather Research Institute (CLRI), Chennai 600 020 for EPR analysis. The authors acknowledge Dr. Maya Raman, Department of Biotechnology, IIT-Madras for assisting in data analysis, and Dr. Suresh Kumar Rayala and Mr. Anuj, Department of Biotechnology, IIT-Madras for providing technical support.

Supplementary data

Electronic supplementary information (ESI) is available. Selected bond lengths and bond angles, and hydrogen bonds geometry relevant to the ligand HL^3 (Tables S1 & S2), selected data of IR, NMR, UV-Vis, PL spectra (Tables S3−S6), CV data (Table S7), selected bond lengths and bond angles by theoretical calculations (Table S8) and figures

showing crystal packing of HL^3 (Fig. S1), NMR spectra (Figs. S2−S10), UV-Vis spectra (Figs. S11−S13), PL spectra (Fig. S14), cyclic voltammograms (Fig. S15 & S16), optimized structure and FMOs of complexes (Figs. S17 & S18), cell viability plots (Figs. S19 & S20), and non-bonding interaction diagrams of complexes docked with EGFR (Fig. S21) are provided as the supplementary material. Crystallographic data have been deposited with the deposition code CCDC 1032819 for the ligand HL^3. Copies of this information may be obtained from The Director, CCDC, 12 Union Road, Cambridge, CB2 1EZ, UK, Fax: +44 1233 336033, E-mail: deposit@ccdc.cam.ac.uk or www.ccdc.cam.ac.uk.

References

[1] A. Kakanejadifard, F. Esna-Ashari, P. Hashemi and A. Zabardasti, *Spectrochim. Acta A*, 2013, **106**, 80–85.

[2] G. J. Roth, A. Heckel, J. T. Kley, T. Lehmann, S. G. Müller, T. Oost, K. Rudolf, K. Arndt, R. Budzinski, M. Lenter, R. R. H. Lotz, M. Schindler, L. Thomas and D. Stenkamp, *Bioorg. Med. Chem. Lett.*, 2015, **25**, 3270–3274.

[3] F.W. Jones, *J. Agric. Food Chem*., 1983, **31**, 190–194.

[4] L. Y. Guo, X. L. Zhang, H. S. Wang, C. Liu, Z. G. Li, Z. J. Liao, B. X. Mi, X. H. Zhou, C. Zheng, Y. H. Li and Z. Q. Gao, *J. Mater. Chem. C*, 2015, **3**, 5412–5418.

[5] I. Jess and C. Nather, *Inorg Chem*., 2003, **42**, 2968–2976.

[6] S. Brooker, J.D. Ewing, T.K. Ronson, C.J. Harding, J. Nelson and D.J. Speed, *Inorg. Chem*., 2003, **24**, 2764–2773.

[7] S. Brooker, S.J. Hay and P.G. Plieger, *Angew. Chem., Int. Ed*., 2000, **39**, 1968–1970.

[8] A. V Komkov, A. S. Komendantova, L. G. Menchikov, E. I. Chernoburova, Y. A. Volkova and I. V Zavarzin, *Org. Lett.*, 2015, **17**, 3734–3737.

[9] N.G. Kandile, M.I. Mohamed, H. Zaky and H.M. Mohamed, *Eur. J. Med. Chem*., 2009, **44**, 1989–1996.

[10] R.R. Harris, L. Black, S. Surapaneni, T. Kolasa, S. Majest, M.T. Namovic, G. Grayson, V. Komater, D. Wilcox, L. King, K. Marsh, M.F. Jarvis, M. Nuss, H. Nellans, L. Pruesser, G.A. Reinhart, B. Cox, P. Jacobson, A. Stewart, M. Coghlan, G. Carter and R.L. Bell, *J Pharmacol. Exp. Ther*., 2004, **311**, 904–912.

[11] S. Ahmad, I.G. Rathish, S. Bano, M.S. Alam and K.K. Javed, *J. Enzyme. Inhib. Med. Chem*., 2010, **25**, 266–271.

[12] E.L. Piatnitski, M.A. Duncton, A.S. Kiselyov, R. Katoch-Rouse, D. Sherman, D.L. Milligan, C. Balagtas, W.C. Wong, J. Kawakami and J.F. Doody, *Bioorg. Med. Chem. Lett*., 2005, **15**, 4696–4698.

[13] A. L. Gavrilova and B. Bosnich, *Chem. Rev*., 2004, **104**, 349–384.

[14] K.R. Grünwald, M. Volpe, P. Cais, G. Gescheidt and N.C. Möschg-Zanetti, *Inorg. Chem*., 2011, **50**, 7478–7488.

[15] D.R. Lide, *CRC Handbook of Chemistry and Physics*, Taylor & Francis, Boca Raton, 88th edn, 2007.

[16] Z. Deng, H.W. Tseng, R. Zong, D. Wang and R.A. Thummel, *Inorg. Chem*., 2008, **47**, 1835–1848.

[17] U. Beckmann and S. Brooker, *Coord. Chem. Rev*., 2003, **245**, 17–29.

[18] M.Weitzer and S. Brooker, *Dalton Trans*., 2005, 2448–2454.

[19] C.X. An, X.R. Li and Z.H. Zhang, *Transit. Met. Chem*., 2009, **34**, 255–261.

[20] S. Eckhardt, *Curr. Med. Chem: Anti-Cancer Agents*, 2002, **2**, 419–439.

[21] F. Rojo, J. Albanell, A. Rovira, J.M. Corominas and F. Manzarbeitia, *Semin. Diagn. Pathol*., 2008, **25**, 245–261.

[22] C. Farina, M. Pinza, A. Cerri and F. Parravinci, *PCT Int. Appl., EP* 274409 A2, 1998.

[23] W.L.F. Armarego and D.D. Perrin, *Purification of Laboratory Chemicals*, Pergamon press. 4th edn, 1996.

[24] Bruker-Nonius, in APEX – II and SAINT – plus (Version 7.06a), Bruker AXS Inc., Madison, Wisconsin, USA, 2004.

[25] A. Altomare, G. Cascarano, C. Giacovazzo and A. Guagliardi, *J. Appl. Crystallogr*., 1993, **26**, 343–350.

[26] M. Sheldrick, *Acta Crystallogr.*, *Sec*., A, 2008, **64**, 112–122.

[27] L.J. Farrugia, *J. Appl. Crystallogr*., 1997, **30**, 565–566.

[28] M.J. Frisch, G.W. Trucks, H.B. Schlegel, G.E. Scuseria, M.A. Robb, J.R. Cheeseman, J.A. Montgomery Jr., T. Vreven, K.N. Kudin, J.C. Burant, J.M. Millam, S.S. Iyengar, J. Tomasi, V. Barone, B. Mennucci, M. Cossi, G. Scalmani, N. Rega, G.A. Petersson, H. Nakatsuji, M. Hada, M. Ehara, K. Toyota, R. Fukuda, J. Hasegawa, M. Ishida, T. Nakajima, Y. Honda, O. Kitao, H. Nakai, M. Klene, X. Li, J.E. Knox, H.P. Hratchian, J.B. Cross, C. Adamo, J. Jaramillo, R. Gomperts, R.E. Stratmann, O. Yazyev, A.J. Austin, R. Cammi, C. Pomelli, J.W. Ochterski, P.Y. Ayala, K. Morokuma, A. Voth, P. Salvador, J.J. Dannenberg, V.G. Zakrzewski, S. Dapprich, A.D. Daniels, M.C. Strain, O. Farkas, D.K. Malick, A.D. Rabuck, K. Raghavachari, J.B. Foresman, J.V. Ortiz, Q. Cui, A.G. Baboul, S. Clifford, J. Cioslowski, B.B. Stefanov, G. Liu, A. Liashenko, P. Piskorz, I. Komaromi, R.L. Martin, D.J. Fox, T. Keith, M.A. Al-aham, C.Y. Peng, A. Nanayakkara, M. Challacombe, P.M.W. Gill, B. Johnson, W. Chen, M.W. Wong, C. Gonzalez and J.A. Pople, Gaussian 03, R1evision D.1, Gaussian, Inc., Pitttsburgh, PA, 2005.

[29] A. D. Becke, *J. Chem. Phys*. 1993, **98***,* 5648–5652.

[30] S. Hemaiswarya and M. Doble, *Phytomedicine*, 2013, **20**, 151–158.

[31] J. Shao, Z.-Y. Ma, A. Li, Y.-H. Liu, C.-Z. Xie, Z.-Y. Qiang and J.-Y. Xu, *J. Inorg. Biochem*., 2014, **136**, 13–23.

[32] M. Raman and M. Doble, *J. Funct. Foods*, 2015, **15**, 354–364.

[33] M. Gavranic, B. Kaitner and E. Mestrovic, *J. Chem. Crystallogr*., 1996, **26**, 23–28.

[34] M. K. Paul, Y. Dilipkumar Singh, N. Bedamani Singh and U. Sarkar, *J. Mol. Struct.*, 2015, **1081**, 316–328.

[35] S. Saydam and E. Yilmaz, *Spectrochim. Acta A*, 2006, **63**, 506 –510.

[36] K. Nakamoto, *Infrared and Raman Spectra of Inorganic and Coordination Compounds: Part – A: Theory and Applications in Inorganic Chemistry*, John Wiley & Sons, Inc., New York, 6th edn, 2009.

[37] R. Bhalla, M. Helliwell and C.D. Garner, *Inorg. Chem*., 1997, **36**, 2944–2949.

[38] S. Ramakrishnan, D. Shakthipriya, E. Suresh, V.S. Periasamy, M.A. Akbarsha and M. Palaniandavar, *Inorg. Chem.*, 2011, **50**, 6458–6471.

[39] P. Purkayastha, G.K. Patra, D. Datta and N. Chattopadhyay, *Indian J. Chem. A*, 2000, **39**, 375–377.

[40] N. Chattopadhyay, A. Mallick and S. Sengupta, *J. Photochem. Photobiol. A*, 2005, **177**, 55–60.

[41] S. Konar, A. Jana, K. Das, S. Ray, S. Chatterjee, J.A. Golen, A.L. Rheingold and S.K. Kar, *Polyhedron*, 2011, **30**, 2801–2808.

[42] L. Wang, W. Qin, X. Tang, W. Dou and W. Liu, *J. Phys. Chem. A*, 2011, **115**, 1609–1616.

[43] B.J. Hathaway, G.N. Bardly and R.D. Gillard, Eds., *Essays in Chemistry*, Academic press, Newport, USA, 1971.

[44] R. Kannappan, S. Tanase, I. Mutikainen, U. Turpeinen and J. Reedijk, *Inorg. Chim. Acta*, 2005, **358**, 383–388.

[45] D.N. Kumar, B.K. Singh, B.S. Garg and P.K. Singh, *Spectrochim. Acta A*, 2003, **59**, 1487–1496.

[46] A. Syamal, *Chem. Edu*., 1985, **62**, 143.

[47] R.L. Carlin and A.J. Vandryneveledt, *Magnetic Properties of Transition Metal Compounds*, Springer-Verlag, New York, 1997.

[48] W.J. Geary, *Coord. Chem. Rev*., 1971, **7**, 81–122.

[49] R.C. Charles, K.M. Geiser-Bush, S.P. Rowley and P.D. Boyle, *Inorg. Chem.*, 1997, **36**, 6401–6408.

[50] I. Fleming, *Frontier Orbitals and Organic Chemical Reactions*, John Wiley and Sons, New York, 1976.

[51] C. Ravikumar, I.H. Joe and V.S. Jayakumar, *Chem. Phys. Lett*., 2008, **460**, 552–558.

[52] L. Padmaja, C. Ravikumar, D. Sajan, I.H. Joe, V.S. Jayakumar, G.R. Pettit and O.F. Nielsen, *J. Raman Spectrosc*., 2009, **40**, 419–428.

[53] N. Tidjani-Rahmouni, N. E. H. Bensiradj, S. Djebbar and O. Benali-Baitich, *J. Mol. Struct.*, 2014, **1075**, 254–263.

[54] D.F.V. Lewis, C. Ioannides and D.V. Parke, *Xenobiotica*, 1994, **24**, 401–408.

[55] P. Thanikaivelan, V. Subramanian, J.R. Rao and B.U. Nair, *Chem. Phys. Lett.,* 2000, **323**, 59–70.

[56] T.S. Xavier, N. Rashid and I. H. Joe, *Spectrochim. Acta A*, 2011, **78**, 319–326.

[57] P. Graidist, M. Martla and Y. Sukpondma, *Nutrients*, 2015, **7**, 2707-2718.

[58] S. Komeda, M. Lutz, A.L. Spek, Y. Yamanaka, T. Sato, M. Chikuma and J. Reedijk, *J. Am. Chem. Soc*., 2002, **124**, 4738–4746.

[59] D. Mahendiran, P. Gurumoorthy, K. Gunasekaran, R. Senthil Kumar and A. K. Rahiman, *New J. Chem.*, 2015, **39**, 7895–7911.

[60] J. Baselga. *Oncologist*, 2002, **7**, 2−8.

[61] M.A. Lemmon and J. Schlessinger, *Cell*, 2010, **141**, 1117–1134.

NEW PYRIDAZINE-BASED BINUCLEAR NICKEL(II), COPPER(II) AND ZINC(II) COMPLEXES AS PROSPECTIVE ANTICANCER AGENTS

Ummer Muhammed Rafi[a], Dharmasivam Mahendiran[a], Azees Khan Haleel[a], Rakesh Pandeet Nankar[b], Mukesh Doble[b], Aziz Kalilur Rahiman*[a].

[a]Post-Graduate and Research Department of Chemistry, The New College (Autonomous), Chennai-600 014, India.

[b] Bioengineering and Drug Design Lab, Department of Biotechnology, Indian Institute of Technology Madras, Chennai-600 036, India.

Table of contents

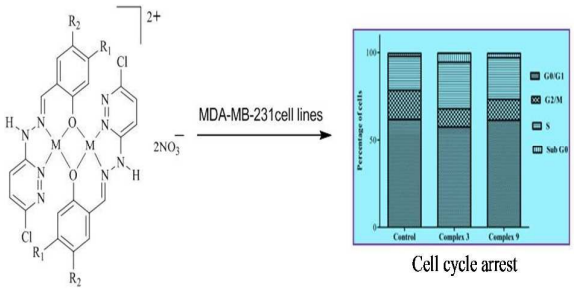

The complexes containing diethylamino substituent exhibit promising cytotoxicity against estrogen receptor (ER) negative MDA-MB-231 breast cancer cell line.